MATHEMATICAL MODELLING OF PLANT ROOT HAIR INITIATION; DYNAMICS OF LOCALIZED PATCHES

V. BREÑA–MEDINA, A.R. CHAMPNEYS, C. GRIERSON, M.J. WARD

Abstract.

A mathematical analysis is undertaken of a Schnakenberg reaction-diffusion system in 1D with a spatial gradient governing the active reaction. This system has previously been proposed as a model of the initiation of hairs from the root epidermis *Arabidopsis*, a key cellular-level morphogenesis problem. This process involves the dynamics of the small G-proteins ROPs which bind to form a single localized patch on the cell membrane, prompting cell wall softening and subsequent hair growth. A numerical bifurcation analysis is presented as two key parameters, involving the cell length and the overall concentration of the auxin catalyst, are varied. The results show hysteretic transitions from a boundary patch to a single interior patch, and to multiple patches whose locations are carefully controlled by the auxin gradient. The results are confirmed by an asymptotic analysis using semi-strong interaction theory, leading to closed form expressions for the patch locations and intensities. A close agreement between the numerical bifurcation results and the asymptotic theory is found for biologically realistic parameter values. Insight into the initiation of transition mechanisms is obtained through a linearized stability analysis based on a non-local eigenvalue problem. The results provide further explanation of the recent agreement found between the model and biological data for both wild-type and mutant hair cells.

1. Introduction. The study of root hairs (RH)s is agriculturally important for understanding and optimisation of both nutrient uptake and anchorage. In addition, the formation and growth of a root hair represents an important problem in single-cell morphogenesis, not least because root hairs are particularly amenable to scientific study due the ease with which they can be imaged; see [43] and references therein. For the model plant *Arabidopsis* there is a wealth of experimental data concerning each step of root hair formation: differentiation of the root epidermis into hair and non-hair cells, see e.g. [44]; the initiation and growth of a single RH from wild-type hair cells; and the behaviour of a wide variety of mutants that generate deformed or multiple hairs per cell, or no hairs at all (see [24, 26]).

This paper concerns the biochemical process by which the process of RH formation is initiated within an *Arabidopsis* RH cell. As depicted in Fig. 1.1(b) the first visible sign that this process has begun is the formation of a patch of small G-proteins known collectively as ROPs (Rhos of plants) at the location on the cell membrane at which the hair will form. Just prior to cell wall bulging to form a root-hair stub, this patch is observed to be 10–20% of the cell length away from the apical (root tip) end of the cell. The process by which a patch of active ROP spontaneously forms in its wild-type position, from where a root hair forms, appears to take place within a timescale of minutes, see e.g. [24]. It appears to be triggered within the growing root as the RH cell reaches a combination of a critical length and a critical overall auxin concentration.

The key feature of a model concerning such an initiation process, as proposed by Payne and Grierson [41], is that the activation step is postulated to be dependent on the concentration of the plant hormone auxin. Although auxin is too small to be imaged on its own, by using the auxin flow model introduced by Kramer [28], Jones *et al.* [24] were able to surmise that there is a decreasing gradient of auxin from the apical end of each RH cell.

Assuming that such a gradient mediates the autocatalytic activation of ROPs, simulations by Payne and Grierson [41] showed that the active-ROP variable tends to form patch-like states towards the apical end, as in Fig. 1.1(b). Moreover, various patch states can be found that show a close qualitative match with observations on the location, width and distribution of multiple hair cells on a variety of mutants. There it is also shown that the effect of too much auxin in young cells is to produce mutants that spontaneously
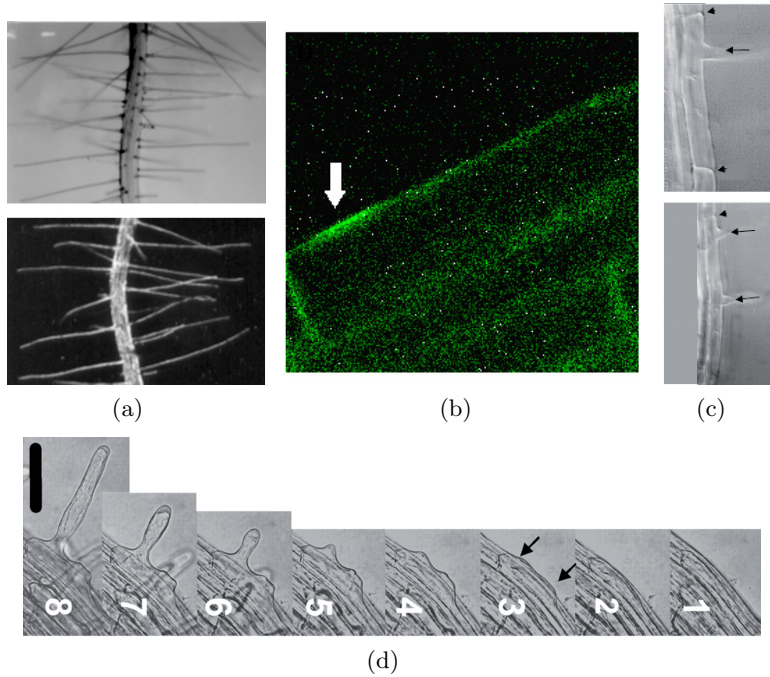
Fig. 1.1: (a) Image of root hair cells of *Arabidopsis*. (b) An apical of surface bound ROP imaged using GFP in wild-type just prior to cell wall bulging. (c) Mutants affected by auxin. On the top panel, the RH site is farther away from the apical end (indicated by the left arrow cap); on the bottom panel, multiple RH locations are initiated simultaneously (indicated by arrows). Figures reproduced from [41]. (d) Mutant which overexpresses the gene *ROP2*; from right to left, numbers indicate successive snapshots at different times. RH initiation sites are indicated by the arrows. The bar represents $75\mu m$. Figure reproduced from [25].

form two or more hairs, in keeping with results in the experimental literature. Other mutant phenotypes which form hairs with different geometries could also be matched in the shape of the underlying ROP patch. The purpose of this paper is to provide a detailed mathematical explanation of these simulation results and to form further biological hypotheses on how the root hair initiation process occurs.

As we shall see, within a given model, asymptotic methods can lead to full parametrisation of qualitative features, such as patch width and instability threshold, that should then enable new experimental hypotheses to be formed and tested. As an example of this, the analysis in §5 below throws light on the observations by Jones and Smirnoff [25] that in multiple root-hair mutants there appears to be a correlation between the proximity to the apical end of the cell and the progress of each hair's tip growth.

The system we study is a generalization of the Schnakenberg model [45], which is one of the most widely studied models of Turing-like pattern formation. Beyond initial Turing instabilities, the model is known to present a rich variety of self-organising dissipative structures, whose dynamics give insights on biological pattern formation from sub-cellular to ecological lengthscales; see, for example, [31] for a review.

There is also an extensive literature on the formation of spatially localized structures in the Schnakenberg model. For instance, existence and asymmetry of spike-like structures [50], stability of symmetric N-spiked steady-states [23], dynamics and self-replication of spot-like structures in 2D [27] have been analysed. Ehrt *et al.* [12, 42] analyse first- and second-order interface interactions providing methods to

describe the location and dynamics of spikes in such a system. Also, the model plays a central role in observation of such structures in chemical reactors see e.g. [11, 48]. Related reaction-diffusion systems such as the Gray–Scott and Gierer–Meinhardt models have also been thoroughly analyzed, see [5, 8, 9, 22, 51] and the references therein. There, in addition to the analysis of the existence and the dynamics of localized solutions, the stability of localized structures has been investigated by analyzing the spectrum of certain non-local eigenvalue eigenvalue problems. These previous studies have focussed on the case where there is no imposed spatial gradient in either the nonlinear kinetics or diffusivities.

Pattern formation in the presence of spatial inhomogeneity in either the reaction kinetics or the diffusivities is less well understood than for the spatially homogeneous case. Preliminary results on the effect of inhomogenities on the Turing instabilities in the Schnakenberg model were considered by Maini and co-workers [1, 30]. Glimm *et al.* [18, 19] analyse reaction-diffusion systems where certain kinetic terms are assumed to be affected by a linear chemical gradient. Page *et al.* [38, 39] explore self-organised spatial patterns in the Gierer–Meinhardt system outside the classical Turing instability regime, allowing the kinetic coefficients to vary either in discrete jumps or via periodic modulation. Similarly, Ward *et al.* [49] analyze a reduced Gierer–Meinhardt system with inhomogeneous linear kinetic terms using matched asymptotics. In addition, far from a Turing perspective, Matties and Wayne [32] prove the existence of stationary and pinned waves in a more general context, by using averaging and homogenization techniques.

In the literature there has been a particular focus on analyzing pinning phenomena, in which localized traveling-wave type solutions get frozen at specific spatial locations as a result of spatial inhomogeneities in the medium. For instance, Heijster *et al.* [47] analyze the effect of a jump-type, externally imposed, heterogeneity on both transition-layer and pulse-type solutions in a generalised FitzHugh–Nagumo system. Nishiura and his collaborators [37, 54] have performed thorough analyses of the effect of such inhomogenities in a three-component reaction-diffusion system and the Gray–Scott system. The focus in these studies is to characterize whether traveling fronts either penetrate through, are reflected from, or are pinned by the inhomogeneity. In Wei and Winter [53] the influence of a discontinuous inhibitor diffusion coefficient on the existence and stability of spikes in a Gierer–Meindhardt system is investigated. We are not aware of any study of the stability and dynamics of localized spikes when the spatial inhomogeneity arises in the nonlinear terms of the reaction kinetics.

In comparison with these previous works, the novel mathematical feature of the present paper is that a parameter gradient multiplies the *nonlinear* terms in the kinetics of the reaction-diffusion system. We analyze the role that this gradient has on the existence, stability, dynamics, and bifurcation structure, of localized spikes for this system.

This outline of this paper is as follows. In §2, we explain a few features of the biology and derive the fundamental system to be studied. We also provide some preliminary analysis and numerical simulation data that point to the existence of localized spike solutions that represent patches of high concentrations of active ROPs. In §3 numerical bifurcation results are given to identify parameter regions where different forms of solution profile exist, and to exhibit the types of instability that cause transitions between them. In §4 a matched asymptotic expansion analysis, in the spirit of Ward and Wei [50], is given to provide analytical predictions of the location and width of single- and multiple-patch states. Then, in §5, we explore thoroughly the *competition instability* of multiple spikes in an $\mathcal{O}(1)$ time-scale regime, in order to derive a critical threshold of the parameters beyond which certain spike-type solutions become unstable. The

asymptotic results for the dynamics and stability thresholds are found to be in close agreement with full numerical results. Finally, §6 contains concluding remarks, discusses biological implications for the work and makes suggestions for future work.

2. Mathematical Model. Rho-family small GTPases are a group of proteins whose main role seems to be that of transmitting chemical signals in order to effect a number of changes inside the cell. Working as molecular "connectors", these proteins shift between active and inactive states. Plants possess a single subfamily of Rho GTPases known as Rho of Plants (ROP) which control a wide variety of cellular processes, see [4] and references within. These biochemical compounds contribute strongly to cellular level processes such as morphogenesis, movement, wound healing, division and, of particular interest here, cell polarity generation [14, 24, 33, 36, 40]. In particular we are interested in the role of ROPs in forming patches that produce local cell outgrowths.

In addition, plant hormones known as *auxins* are thought to play a crucial role in almost all aspects of a plant's life. Auxins stimulate growth, and regulate fruit setting, budding, side branching, and the formation of delicate flower parts among many other morphogenic tissue-level responses. In a sense, RH outgrowth is one of the simplest and easiest studied effects that is stimulated by auxin [24, 33].

Root hair cells are intercalated with cells that do not develop RHs. Specification from a recently-formed epidermal cell into a RH cell or non-RH cell is a topic which has warranted particular attention [44] as it leads to a better understanding of cell-type patterning generally in plants. As is stated in [21, pp. 3], patterning information is provided at an early stage in epidermis development, immature epidermal cells destined to become RH cells are distinguished from their counter part, non-RH cells, prior to hair outgrowth. The differentiating RHs cells present a greater cell division rate, smaller length, greater cytoplasmic density, lower vacuolation rate and distinguishable cell wall epitopes; see also [2, 10, 16, 17, 26].

Arabidopsis RHs normally develop at $1 \mu m/min$, and stop growing when a critical length is reached. At this point, the cytoplasm at the tip spreads out and the vacuole expands. Also, it has been experimentally observed that ROPs are involved in branching and deformation of tips (see e.g. [26]). Genetic analysis of these processes has identified specific proteins that are strongly engaged in mechanisms of RH initiation and tip growth (see [15, 21] and the references therein). In addition, *The Arabidopsis Information Resource* is a database of genetic and molecular biology data for the model higher plant Arabidopsis thaliana [46]. There data for many genes that particularly affect RHs are given. However, our focus will be to consider a selection of them that illustrate features of ROP interactions pertinent to initiation and ROP patch location dynamics.

2.1. ROP Kinetics. Each ROP protein comes in two states: activated and inactivated. Inactive ROP may be either bound to the cell membrane or in the *cytoplasm*. In our model we shall not model the binding mechanism *per se* but shall differentiate only between the active form which can only diffuse within the confines of the cell membrane, and the inactive form, the majority of which is free to diffuse in the 2D cytoplasm. We will approximate the long-thin RH cell by a 1D domain, of length L, and shall distinguish between membrane and cytoplasm only through separate diffusion constants. That is we model a mathematical domain $(z, T) \in [0, L] \times \mathbb{R}^+ \cup \{0\}$ and let $\tilde{U}(z, T)$ represent the concentration of *bound/active* and $\tilde{V}(z, T)$ the *unbound/inactive* ROP. Our model also reflects the fact that the kinetic processes occur considerably faster than the changes to cell length and auxin concentration levels. Therefore, we shall
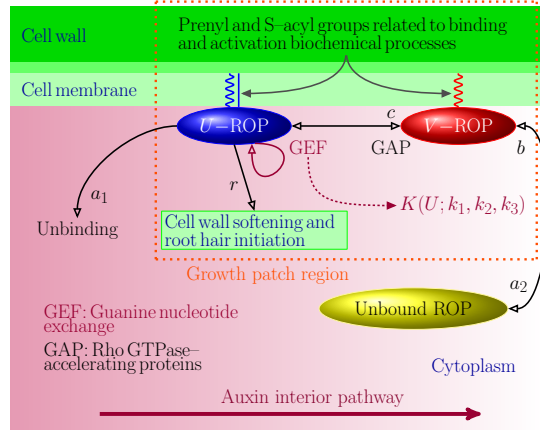
Fig. 2.1: Sketch of the binding process where autocatalytic activation and catalysis effect by auxin are coloured in purple.

assume that the latter are effective bifurcation parameters that vary quasi-statically.

The transition between inactive and active forms is known to be controlled by intracellular signalling through so-called ROP-regulators: *guanine nucleotide exchange factors* (GEF) that catalyse ROP activation and *GTPase-activating protein* (GAP) that deactivate ROPs. We therefore model the switching fluctuation between both densities as depicted in Fig. 2.1. That is, the active Rho state is deactivated at a rate κ_{GAP}, and equivalently inactive Rhos are activated at rate κ_{GEF}. These rates depend upon the presence of GEFs or GAPs respectively. Fig. 2.1 shows the entire process schematically; the auxin gradient is represented by shading of the cytoplasm, where the arrow indicates decreasing concentration.

It is widely postulated in models of similar Rho-proteins in yeast and mammals, that the GEF activation step involves positive feedback (autocatalysis) whereas the GEF step is thought to be passive; see for example [34].

Payne and Grierson [41] characterized a transition between active and inactive state of ROPs via GEFs and GAPs by taking $\kappa_{GEF}(\tilde{U}) \equiv \kappa_1 + \kappa_2 \tilde{U}^2$ and allowing only one species of ROP to be modelled. This simplification can be justified as follows. In plants, although there are several different kinds of ROP, their activation is not thought to involve cross talk. Also, by including a constant production rate of the inactive ROP and a constant probability of recycling or further processing of active ROP, there is no need for a cross-talk or Hill function kinetics explicit saturation term. In fact, as shown in Proposition 2.2 below, the total amount of active ROP is a conserved quantity in any steady solution.

Moreover, according to Jones *et al.* [24] and Grieneisen *et al.* [20], there is experimental evidence which suggests that a spatially decaying (as z increases) gradient of auxin, as postulated by Payne and Grierson, modulates the autocatalytic step. That is, we suppose then the constant κ_2 is spatially dependent: $\kappa_2 = k_{20}\alpha(z/L)$. Here k_{20} measures an overall concentration of auxin and $\alpha(z/L)$ is a smooth function that represents the spatial distribution of auxin, normalised so that

$$\alpha(0) = 1, \qquad \alpha'(x) < 0, \quad \text{for all } x \in (0, 1).$$

In all the computations that follow, we take the function $\alpha(x) = e^{-\nu x}$, $\nu = 1.5$, which models the steady

5

state concentration of a leaky diffusion process (see [41]). However, simulation results were found to be insensitive to different piecewise-smooth non-increasing functional forms of α, for the same $\alpha(0) - \alpha(1)$.

In contrast, we suppose that $\kappa_1 = k_1$ a constant. All other processes are supposed to follow the simple law of mass action, with the GEF-induced deactivation/unbinding rate given by a constant $\kappa_{GAP} = c$. Furthermore, b is assumed to be the constant rate of production of inactive ROP and r the rate at which active ROP is recycled or used up to produce other complexes, including those that go on to produce cell wall softening.

2.2. Fundamental Model. Under the above assumptions, and by using the law of mass action allied to Fick's law of diffusion in a standard way, we obtain the reaction-diffusion system

$$\text{Bound-active ROP:} \quad \frac{\partial \tilde{U}}{\partial T} = D_1 \frac{\partial^2 \tilde{U}}{\partial z^2} + k_{20}\alpha(z/L)\tilde{U}^2\tilde{V} - (c+r)\tilde{U} + k_1\tilde{V}, \tag{2.1a}$$

$$\text{Unbound-inactive ROP:} \quad \frac{\partial \tilde{V}}{\partial T} = D_2 \frac{\partial^2 \tilde{V}}{\partial z^2} - k_{20}\alpha(z/L)\tilde{U}^2\tilde{V} + c\tilde{U} - k_1\tilde{V} + b. \tag{2.1b}$$

We impose the no-flux boundary conditions $\tilde{U}_z = 0$, $\tilde{V}_z = 0$ at $z = 0, L$, which supposes that, unlike the small molecule auxin, the large ROPs do not diffuse through the cell wall.

The Schnakenberg system can be recovered from (2.1) by setting k_1 and c to zero, adding a constant production term to $\tilde{U}$-equation, and taking $\alpha \equiv 1$; this transformation can be seen as an homotopy between both systems. Furthermore, both systems are derived from simple reactions where an autocatalytic process is present. Both models can effectively be thought of as showing activator-substrate behaviour. That is, as we shall see in our later numerical and analytical results, in activation regions the activator aggregates so that the substrate is consumed quickly, which results in substrate valleys occuring at activator peaks.

As already stated, we presume that bound ROPs diffuse more slowly, so that the diffusion coefficients D_1 and D_2 are assumed to satisfy $D_1 \ll D_2$. Payne and Grierson [41] postulated the following plausible parameter values:

$$D_1 = 0.1\frac{\mu m^2}{s}, \quad D_2 = 10\frac{\mu m^2}{s}, \quad b = 0.01\frac{\text{con}}{s}, \quad r = 0.01\frac{\text{con}}{s},$$

$$c = 0.1\frac{\text{con}}{s}, \quad k_1 = 0.01\frac{\text{con}}{s}, \quad L = 50\mu m, \quad k_{20} \in [0.01, 1], \tag{2.2}$$

which, with $k_{20} = 0.1\text{con}^2/s$, were found to match well the time and length scales associated with RH formation in wild type *Arabidodpsis*, where the fundamental units of space and time are μm and *sec*, and concentrations are measured with respect to an arbitrary datum (con). In the original model (see [41]) the cell length L and auxin concentration k_{20} are known to be slowly transiently increasing during the root hair initiation process. To simulate this Fig. 2.2 & 2.3 show the effect of such transient sweeps within the cell. In this paper we shall consider the auxin concentration k_{20} and cell length L to be the primary bifurcation parameters.

2.3. Initial Parameter Sweep. The computational results in [41], based on experimental recordings, suggest that a single patch of high active ROP concentration occurs during a period of root development when the length of the RH cell increases to about $L = 50$–$60\mu m$ and the auxin concentration parameter k_{20} is in the range 0.1–$0.2\text{con}^2/s$. To ease notation, we will not specify units from now on. Fig. 2.2 shows spatio-temporal plots of solutions to (2.1), computed using XPPAUT [13] with parameters held to their
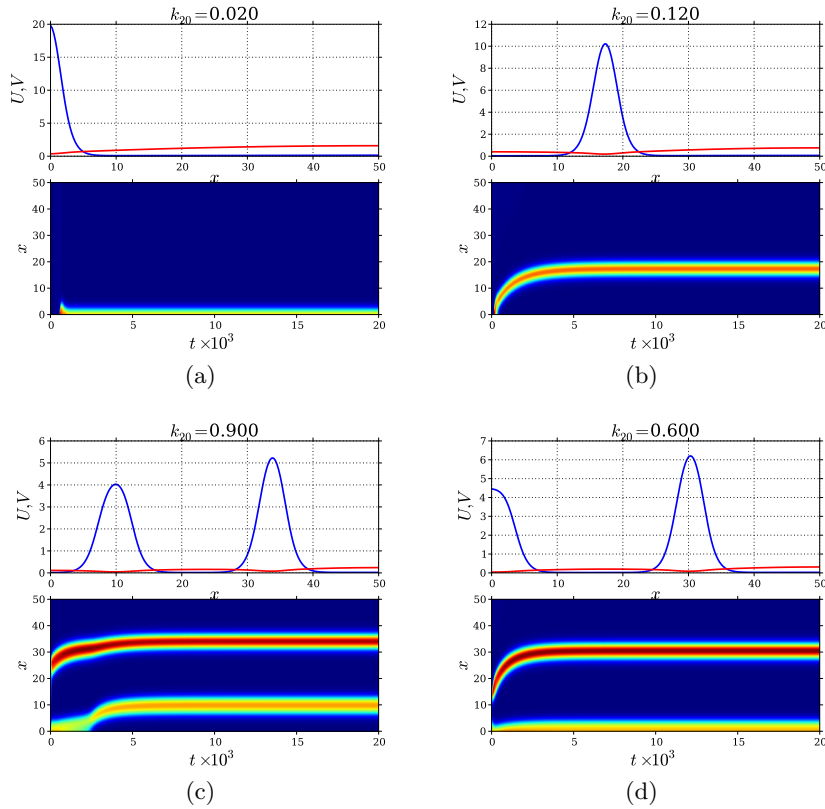
Fig. 2.2: Final profile and patch dynamics, with no variation of parameters, for (a) boundary patch, (b) an interior patch, (c) double patch and (d) boundary and interior patch. U- and V-final profiles are plotted in blue and red respectively (top panels in (a)–(d)), and U-spike solutions on heat bar scale. Parameter values as in (2.2).

values in (2.2). We note four distinct types of steady state solution. These comprise, selecting $L = 50$ for specific k_{20} parameter values, a *boundary patch* (Fig. 2.2(a)), a *single interior patch* (Fig. 2.2(b)) and *multiple interior patch* (Fig. 2.2(c)); in addition, a another kind of multiple-patch solution can also be observed, a *boundary and interior patch* (Fig. 2.2(d)). Further numerical results (not shown) indicate that for yet higher values of L and k_{20} n-patch states can be observed with a broad trend that n increases with L or k_{20}.

For each of these solution, by a "patch" we mean a region in which there is a localized spike in concentration of active ROP $\tilde{U}$, while the concentration of $\tilde{V}$ varies globally across the domain, but with a trough whenever $\tilde{U}$ has a peak.

The left-hand panels of Fig. 2.3 show what happens under the biologically more realistic mechanism of gradual increase of *both* cell length and auxin concentration over the course of about 30 minutes, which is the timescale under which root hairs are thought to emerge. For the upper panel (Fig. 2.3(a)), a single interior patch emerges, as would occur in wild type. In Fig. 2.3(c), L and k_{20} are increased more rapidly so that the single patch splits into two interior patches which would represent the behaviour of a mutant that over expresses auxin.

An interesting phenomenon is seen in the right-hand panels of Fig. 2.3. If the auxin and cell length
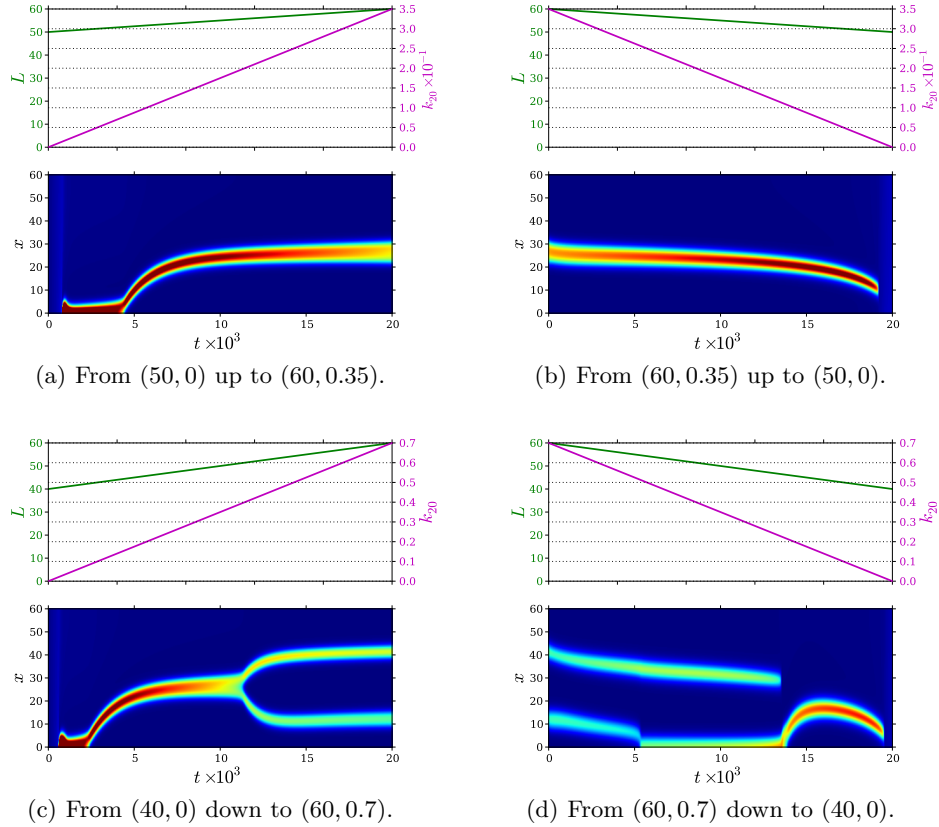
(a) From $(50, 0)$ up to $(60, 0.35)$.

(b) From $(60, 0.35)$ up to $(50, 0)$.

(c) From $(40, 0)$ down to $(60, 0.7)$.

(d) From $(60, 0.7)$ down to $(40, 0)$.

Fig. 2.3: Hysteresis for two different transition speeds varying growth patch region length and auxin acceleration rate. The shift in the L and k_{20} parameters are plotted in green and purple, and the intensity of the U field is plot on a heat scale.

variation is reversed, we see that the point of instability of the two patch or the one-patch state does not occur at the same levels as the equivalent phenomenon under parameter increase. In other words there is hysteresis in the formation of the patterned states. Also, the interior patch seems to endure longer, as seen in Fig. 2.3(b), than multiple interior patch in transition, as shown in Fig. 2.3(d). This suggests that effectively an interior patch tends to be more persistent than other states. This gives us an initial insight on the biological robustness of the pattern formation mechanism; once a process of patch formation has set in under increase of a parameter, it would not be undone by a momentary reduction of that parameter. We shall study the bifurcations underlying this hysteresis in §3 below.

Note also from these results that there appear to be several asymptotic scales; there is a definite length scale associated with the size of the active ROP patches, there is a timescale associated with slow drift of patches and a more rapid timescale associated with formation or instability of the patches. These observations give a clue to the form of multiple scale asymptotic analysis with which we can explain these results. In that direction, we shall consider next an asymptotic rescaling of the model.

2.4. Asymptotic Rescaling and Parameter Identification. In order to analyze (2.1), it is helpful to introduce a change of variables. First, we identify $D_1/(c + r)$ and D_2/k_1 as the effective diffusion
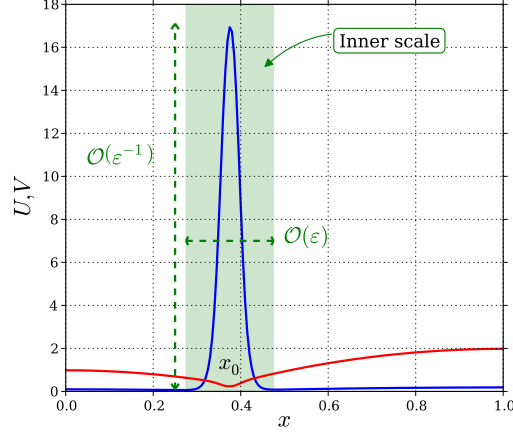
Fig. 2.4: Schematic plot of the inner and outer solution for a steady-state solution. The active-component U has a patch, whereas V has a global variation across the domain.

coefficients for $\tilde{U}$ and $\tilde{V}$, respectively. Hence we rescale via

$$\tilde{V} = \frac{b}{k_1}V\,, \qquad \tilde{U} = \frac{(c+r)k_1}{k_{20}b}U\,. \tag{2.3}$$

Then, upon defining nondimensional time and space variables via

$$t = (c+r)T, \qquad x = \frac{z}{L}$$

so that $x \in [0,1]$. We introduce a small parameter ε by $\varepsilon \equiv \sqrt{D_1/L^2(c+r)}$. As shall be seen below in Proposition 2.2, we conclude that if $U \ll 1$ away from the patch, then $U = \mathcal{O}\left(\varepsilon^{-1}\right)$ in the core of the patch, and as a consequence $V = \mathcal{O}(\varepsilon)$ near a patch (see Fig. 2.4). This formal scaling argument motivates the introduction of the new variables u, and v, defined by

$$U \equiv \varepsilon^{-1}u\,, \qquad V \equiv \varepsilon v\,.$$

In terms of these new variables, we obtain the *rescaled equations*

$$u_t = \varepsilon^2 u_{xx} + \alpha(x)u^2 v - u + \frac{\varepsilon^2}{\tau\gamma}v\,, \tag{2.4a}$$

$$\varepsilon\tau v_t = D_0 v_{xx} + 1 - \varepsilon v - \varepsilon^{-1}\left(\tau\gamma\left(\alpha(x)u^2 v - u\right) + \beta\gamma u\right)\,, \tag{2.4b}$$

on $0 < x < 1$ and $t > 0$, with $u_x = v_x = 0$ at $x = 0,1$, and $D_0 \equiv \varepsilon D$ which comes from balancing terms in (2.4b).

Here, the dimensionless parameters are given by

$$\varepsilon^2 \equiv \frac{D_1}{L^2(c+r)}\,, \qquad D \equiv \frac{D_2}{L^2 k_1}\,, \qquad \tau \equiv \frac{c+r}{k_1}\,, \qquad \beta \equiv \frac{r}{k_1}\,, \tag{2.5}$$

and the primary bifurcation parameter is

$$\gamma \equiv \frac{(c+r)k_1^2}{k_{20}b^2}\,. \tag{2.6}$$

9

Original	Re-scaled		Original	Re-scaled
$D_1 = 0.1$	$\varepsilon^2 = 3.6 \times 10^{-4}$		$D_1 = 0.1$	$\varepsilon^2 = 2.3 \times 10^{-5}$
$D_2 = 10$	$D = 0.4$		$D_2 = 50$	$D = 0.5$
$L = 50$			$L = 100$	
$k_1 = 0.01$	$\tau = 11$		$k_1 = 0.01$	$\tau = 44$
$b = 0.01$	$\beta = 1$		$b = 0.005$	$\beta = 4$
$c = 0.1$			$c = 0.4$	
$r = 0.01$			$r = 0.04$	
$k_{20} = 0.01 \ldots 1.0$	$\gamma = 11 \ldots 0.11$		$k_{20} = 0.045 \ldots 40$	$\gamma = 39.1 \ldots 0.04$
(a) **Parameter set** (2.2)			(b) **Parameter set** (2.7)	

Table 2.1: The two parameter sets in the original and re-scaled variables.

Note that $\gamma \propto 1/k_{20}$ so that an increase of auxin corresponds to a decrease of γ. Similarly the parameter $D_0 \propto 1/L^2$ and so we can consider D_0 to be a secondary bifurcation parameter with a decrease in D_0 representing cell lengthening.

The form in (2.4) assumes that $\varepsilon \ll 1$ and that each of the other parameters are $\mathcal{O}(1)$ as $\varepsilon \longrightarrow 0$. Table 2.1(a) shows the original parameter values (2.2) and equivalent re-scaled set of parameter values. Note that the assumed asymptotic scaling is somewhat questionable; $1/\varepsilon \approx 50$ which is similar in magnitude to τ and γ which are assumed to be $\mathcal{O}(1)$. Nevertheless, in what follows we shall find that the asymptotic analysis produces a more than acceptable match with the numerical results.

In order to categorically demonstrate the validity of the results in the asymptotic limit $\varepsilon \to 0$, we shall also consider a second set of parameter values

$$D_1 = 0.1 \frac{\mu m^2}{s}, \quad D_2 = 50 \frac{\mu m^2}{s}, \quad b = 0.005 \frac{\text{con}}{s}, \quad r = 0.04 \frac{\text{con}}{s}, \tag{2.7}$$
$$c = 0.4 \frac{\text{con}}{s}, \quad k_1 = 0.01 \frac{\text{con}}{s}, \quad L = 100 \mu m, \quad k_{20} \in [0.045, 40],$$

which are a small adjustment from those in (2.2) and well within the bounds of biological plausibility, but for which the asymptotic description is more clearly valid, see the Table 2.1(b). For this second set of parameters we shall find a very close agreement between the asymptotic theory and numerics.

2.5. Preliminary Results. We are interested in steady state solutions to (2.4). At first sight, it would seem that the model (2.4) with $\varepsilon \ll 1$ is well set up for pattern formation through Turing bifurcations. Indeed, a wide range of biological pattern formation problems have been studied from the viewpoint of Turing instability analysis around a spatially homogeneous steady-state [29, 35].

To begin such an analysis, consider the homogeneous problem $\alpha(x) \equiv 1$. For either of the parameter sets (2.2) or (2.7), as the auxin concentration k_{20} is increased from zero, or equivalently the parameter γ is decreased to zero, it is straightforward to see that there is a series of Turing bifurcations (pitchforks) to patterns of different wavelengths. However, a lengthy but elementary calculation shows:

Proposition 2.1. *The homogeneous steady state*

$$U = \frac{1}{\beta\gamma}, \qquad V = \frac{\beta\tau\gamma}{\beta^2\gamma + \tau}$$

of (2.4) with $\alpha \equiv 1$ under either parameter set (2.2) or (2.7) is stable for γ sufficiently large. As γ is

decreased to zero there are an infinite number of Turing bifurcations, of increasing wavenumber, the first few of which are subcritical.

Therefore all small-amplitude periodic patterns are unstable. Moreover, straightforward numerical continuation reveals that all these bifurcating branches undergo a further fold bifurcation. After the fold the pattern takes on a spike-like form, constisting of a number of large peaks of U.

What shall interest us in the next section is to numerically find equivalent steady-state solutions for the inhomogeneous problem. In this case there is no trivial steady state to consider bifurcations from. Nevertheless, we note the following conservation principle for steady state solutions of (2.4), which is independent of the form of $\alpha(x)$.

Proposition 2.2. *Any steady-state solution $(U(x,t), V(x,t)) = (U_0(x), V_0(x))$ of the system (2.4) is such that*

$$\bar{U} \equiv \int_0^1 U_0 \, dx = \frac{1}{\beta\gamma} \, . \tag{2.8}$$

Proof. To derive this result, we set $U_t = 0$ and $V_t = 0$ in (2.4), and integrate (2.4a) over the domain and use the Neumann boundary conditions to obtain the equation $\int_0^1 \left[\alpha(x)U_0^2 V_0 - U_0\right] dx = -\frac{1}{\tau\gamma}\int_0^1 V_0 \, dx$. Then, upon using this identity in the expression that results from integrating (2.4b) over the domain we readily obtain (2.8). ∎

This result shows that the total amount of the bound ROP in the patch region depends only upon the constant production and removal rates of ROP, that is, in the unscaled variables $\bar{U} = b/r$. This observation means that the active ROP concentration remains constant no matter how many patches it forms. From a mathematical viewpoint, as has seen above, Proposition 2.2 led to a proper re-scaling for a multiple-scale asymptotic analysis.

3. Numerical Bifurcation Analysis. We next turn to numerical bifurcation analysis to compute steady state solutions to (2.4). In order to provide comparison with other studies that show biological data, all results will be presented in the unscaled system (2.1) using parameter set (2.2). The principal bifurcation parameters will be k_{20}, representing the overall concentration of auxin, and L the cell length. We are interested in identifying and analysing the bifurcations that cause the transitions already observed under slow sweeps in these parameters.

The numerical results have been produced using AUTO [7] applied to the steady-state problem which is a two-point boundary-value problem (BVP). We have augmented this analysis with computations of the temporal stability of solutions, using direct numerical simulation in XPP (cf. [13]) and computation of the spectrum of the discretised steady-states using MATLAB. To perform the spectral computation we used a standard three-point stencil on a uniform grid to discretize the Laplacian; we therefore obtain the operator $\mathbf{L_W} \equiv \mathbf{D} + \mathbf{F}'(\mathbf{W}_0)$, where $\mathbf{D} \equiv \text{diag}\left(\varepsilon^2 \partial_{xx}, D\partial_{xx}\right)$, and $\mathbf{F}'(\mathbf{W}_0)$ is the Jacobian matrix evaluated at $\mathbf{W}_0 = (U_0, V_0)$, a steady-state solution to the BVP. Then we compute the eigenvalues of the discretized operator. Stable solutions have all eigenvalues in the left-half of the complex plane.

Initial solutions for the BVP were found by computing branches that bifurcate from the trivial solution of the homogeneous problem with $\alpha \equiv 1$ and then using a homotopy method to continue these into solutions of the inhomogeneous problem.
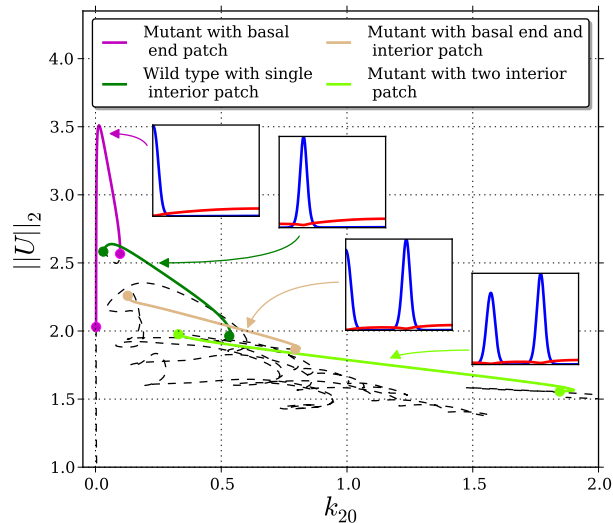
Fig. 3.1: Bifurcation diagram varying k_{20}: branches of boundary patch, single-interior patch, boundary-and-interior patch and two-interior patch; stable solutions are shown as solid lines, unstable solutions as dashed lines and points instability points by filled circles. Parameter set as given in Table 2.1(a).

Fig. 3.1 shows a bifurcation diagram for which the L_2-norm measure. Interior single patch, boundary patch, boundary and interior patch and two interior patch branches are identified. We augment this analysis with the results of stability computations from which we identify stable solutions. One clear feature in the bifurcation structure of these solutions is that a large number of solution branches appear to lie on a single connected curve in the bifurcation diagram (reminiscent of so-called homoclinic snaking [3, 6] on a finite domain). Broadly speaking, as k_{20} increases the number of active-ROP patches in the solution increases. Most solutions for large k_{20} are unstable. However, there appears to be at least one stable branch for each k_{20}-value and regions of stability tend to overlap. All instabilities were found to occur via fold bifurcations, although we do note a slight discrepancy between the steady-state analysis and the stability computations on the location of the initial instability for very low k_{20}-values. There is the suggestion from the computations that there may be a Hopf bifurcation very close to the fold, which we shall not explore in detail further here.

Fig. 3.2(a) shows the position of the global U-maximum of the single interior spike as a function of the bifurcation parameter for both parameter sets in Table 2.1(a) and Table 2.1(b). We note that patch is localized nearer to the boundary for low values of k_{20}. This indicates that the auxin actively controls the position of the patch from which the root hair will grow. This will also be explored using asymptotic analysis in §4. There we shall compare our theoretical results with the numerical ones presented in this section. See in Fig. 3.2(b) a comparison between parameter sets in Table 2.1(a) and Table 2.1(b) for the boundary-patch and single-interior-patch branches.

It is useful to augment these results with two-parameter continuation of the fold curves which give the stability boundaries of the main stable solutions we have identified, the boundary patch, interior patch, boundary and interior patch and two interior patch patterns. Fig. 3.3 shows such a diagram under variation of two parameters that are thought biologically to control the process – namely auxin concentration k_{20}
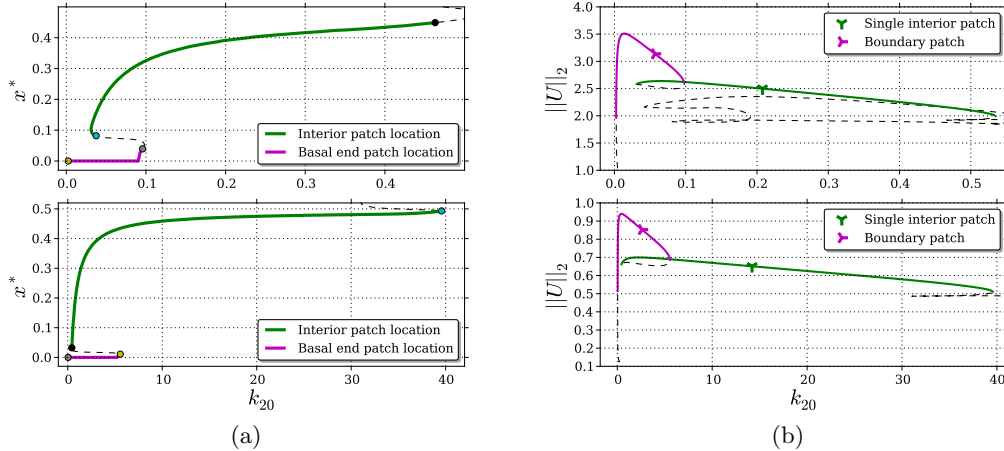
Fig. 3.2: (a) The simplest parts of the bifurcation diagram in which the solution measure is the x-location of the global maximum of U. Dots represent fold points. (b) Comparison of the bifurcation diagram for the boundary-patch and single-interior-patch branches. Parameters values as given in Table 2.1(a) (top panels) and Table 2.1(b) (bottom panels).

and cell length L. It reveals that there are windows where more than one kind of stable solutions can co-exist, this is because branches overlap in a sort of *creation-annihilation cascade*. This organisation explains the hysteretic transitions already seen in Fig. 2.3. The parameter sweeps in Figs. 2.3(a)–2.3(b) and Figs. 2.3(c)–2.3(d) are represented by lines labeled as (A) and (B), respectively.

Note how the bifurcation diagram explains the transitions observed in both simulations. For the first case, in Fig. 2.3(a) the boundary patch onset curve appears at very small k_{20} values, causing an immediate bifurcation from no pattern to a boundary patch. The next transition, upon increase of auxin and length occurs upon crossing the boundary patch annihilation curve, yielding a bifurcation in which the patch jumps into the interior. Notice that the red sweep stops just before single interior annihilation curve meaning that the interior patch state remains. If the parameter sweep is reversed, as in Fig. 2.3(b) note that the interior patch state remains for longer, until the onset curve of that state, which occurs at lower auxin and length values than the annihilation of the boundary patch state.

For the second parameter sweep, the auxin and length increase to higher values and cross the annihilation curve of the single interior patch. This causes a transition into a two interior patch region, see Fig. 2.3(c). On the other hand, going backwards as in Fig. 2.3(d) implies transitions occur not at the annihilation curves, but at the onset curves for each kind of pattern.

4. Asymptotic Analysis; Patch Location. Our numerical study in the previous section has suggested that there should exist wave-pinned solutions in which localized patches, or spikes, of the active component U occur in one or more locations. In order to study such spatial patterns, we will adapt the methodology of Ward *et al.* [12, 22, 23, 42, 49, 50] to construct an asymptotic solution. The strategy there is to find steady-state and quasi-steady-state solutions with localized patches such that for $\varepsilon \ll 1$ the active component is approximately constant except in the patch regions. The existence of a localized solution is a consequence of a short-range activation process, where the inactive component V plays the
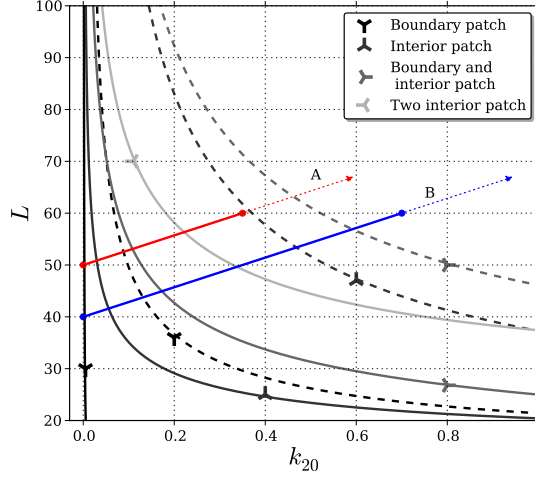
13

Fig. 3.3: Length and auxin 2-parameter continuation of the fold points in Fig. 3.1. Onset (solid) and destruction (dashed) curves are coloured according to each solution type. Transition sweeps shown in (A) Fig. 2.3(a)–2.3(b) and (B) Fig. 2.3(c)–2.3(d). Other parameters are as in Table 2.1(a).

role of long-range substrate. The novelty in our analysis will be to determine how the spatial gradient $\alpha(x)$ controls the locations of the patches.

4.1. Single Patch Solution. In this subsection we use the method of matched asymptotic expansions to construct both a steady-state and a quasi-steady-state single patch solution. In this procedure, an inner solution near the patch is constructed centred on an as yet undefined spatial position x_0 that is asymptotically matched to an outer solution defined away from an $\mathcal{O}(\varepsilon)$ distance from x_0 (see Fig. 2.4).

In the inner region, we seek an asymptotic expansion for $u(\xi)$ and $v(\xi)$ as

$$u = u_0 + \varepsilon u_1 + \cdots, \qquad v = v_0 + \varepsilon v_1 + \cdots, \quad \xi \equiv \varepsilon^{-1}\left(x - x_0\left(\eta\right)\right). \tag{4.1}$$

Here $\eta = \varepsilon^p t$ is a slow time-scale where p is to be found. Upon substituting this expansion into (2.4), we obtain on $-\infty < \xi < \infty$ that

$$-\varepsilon^{p-1}\frac{dx_0}{d\eta}u_\xi = u_{\xi\xi} + \left(\alpha(x_0) + \varepsilon\alpha'(x_0)\xi + \cdots\right)u^2 v - u + \frac{\varepsilon^2}{\tau\gamma}v, \tag{4.2a}$$

$$-\varepsilon^{p+2}\tau\frac{dx_0}{d\eta}v_\xi = D_0 v_{\xi\xi} - \varepsilon\tau\gamma\left(\left(\alpha(x_0) + \varepsilon\alpha'(x_0)\xi + \cdots\right)u^2 v - u\right) - \varepsilon\beta\gamma u + \varepsilon^2 - \varepsilon^3 v. \tag{4.2b}$$

A distinguished limit occurs in (4.2a) when $p = 2$, so that the slow time scale is $\eta = \varepsilon^2 t$. Then, to leading-order we obtain from (4.2) that

$$u_{0\xi\xi} + \alpha(x_0)v_0 u_0^2 - u_0 = 0, \qquad v_{0\xi\xi} = 0. \tag{4.3}$$

At next order, we obtain on $-\infty < \xi < \infty$ that u_1 and v_1 satisfy

$$u_{1\xi\xi} - u_1 + 2\alpha(x_0)v_0 u_0 u_1 + \left(\alpha(x_0)v_1 + \alpha'(x_0)\xi v_0\right)u_0^2 = -\frac{dx_0}{d\eta}u_{0\xi}, \tag{4.4a}$$

$$\frac{D_0}{\tau\gamma}v_{1\xi\xi} - \alpha(x_0)v_0 u_0^2 + u_0 - \frac{\beta}{\tau}u_0 = 0. \tag{4.4b}$$

For (4.3) we impose that $u_0 \to 0$ and that v_0 is bounded as $|\xi| \to \infty$.

14

4.1.1. Quasi-Steady-State Solution. We first construct a quasi-steady-state solution. To leading order we obtain from the second equation in (4.3) that v_0 is a constant, and so we define v^0 by

$$v^0 \equiv v_0(\xi = 0).$$

Then, from the first equation in (4.3) we obtain

$$u_0 = \frac{w}{\alpha(x_0)v^0}, \qquad w \equiv \frac{3}{2}\operatorname{sech}^2\left(\frac{\xi}{2}\right), \tag{4.5}$$

where w is the homoclinic of $w_{\xi\xi} - w + w^2 = 0$ (see [23]).

Returning to the outer-scale system (2.4), the steady-state solutions of this problem satisfy

$$\varepsilon^2 u_{xx} + \alpha(x)u^2 v - u + \frac{\varepsilon^2}{\tau\gamma}v = 0, \tag{4.6a}$$

$$D_0 v_{xx} + 1 - \varepsilon v = \varepsilon^{-1}\left(\tau\gamma\left(\alpha(x)u^2 v - u\right) + \beta\gamma u\right), \tag{4.6b}$$

subject to $u_x = v_x = 0$ at $x = 0, 1$. In the outer region, where $|x - x_0| \gg \mathcal{O}(\varepsilon)$, we obtain from (4.6a) that $u = \tilde{u}_0 + o(1)$ and $v = \tilde{v}_0 + o(1)$ where $\tilde{u}_0 = \varepsilon^2 \tilde{v}_0/\tau\gamma$, which is obtained from making use of the matching condition with (4.5) as $\xi \to \pm\infty$. Therefore, from (4.6b), we obtain in the outer region $|x - x_0| \gg \mathcal{O}(\varepsilon)$ that $\tilde{v}_0$ satisfies

$$D_0 \tilde{v}_{0xx} = -1 + \varepsilon\tilde{v}_0 - \varepsilon^{-1}\tau\gamma\left(\frac{\varepsilon^2}{\tau\gamma}\tilde{v}_0 + \mathcal{O}\left(\varepsilon^4\right)\right) + \frac{\varepsilon\beta}{\tau}\tilde{v}_0 \sim -1 + \mathcal{O}(\varepsilon). \tag{4.7}$$

To determine the appropriate jump condition for $\tilde{v}_0$ across $x = x_0$, we use the leading-order inner solutions $v \sim v^0$ and $u \sim w/\alpha(x_0)v^0$, as given by (4.5), to calculate the right-hand side of (4.6b) in the sense of distributions. In this way, we obtain that

$$\frac{\tau\gamma}{\varepsilon}\left(\alpha(x)u^2 v - u\right) + \frac{\beta}{\varepsilon}\gamma u$$

$$\longrightarrow \left(\frac{\tau\gamma}{\alpha(x_0)v^0}\int_{-\infty}^{\infty}\left(w^2 - w\right)d\xi + \frac{\beta\gamma}{\alpha(x_0)v^0}\int_{-\infty}^{\infty}w\,d\xi\right)\delta(x - x_0),$$

where $w = w(\xi)$ is given in (4.5). Upon calculating $\int_{-\infty}^{\infty}w^2\,d\xi = \int_{-\infty}^{\infty}w\,d\xi = 6$, the result above reduces to

$$\varepsilon^{-1}\tau\gamma\left(\alpha(x)u^2 v - u\right) + \varepsilon^{-1}\beta\gamma u \longrightarrow \frac{6\beta\gamma}{\alpha(x_0)v^0}\delta(x - x_0). \tag{4.8}$$

Therefore, we conclude from (4.6b), (4.7), and (4.8), that the leading-order outer approximation for v satisfies

$$D_0 \tilde{v}_{0xx} = -1 + \frac{6\beta\gamma}{\alpha(x_0)v^0}\delta(x - x_0), \quad 0 < x < 1; \quad \tilde{v}_{0x}(0) = \tilde{v}_{0x}(1) = 0. \tag{4.9}$$

To determine v^0 we integrate (4.9) over the domain, while using $\tilde{v}_{0x} = 0$ at $x = 0, 1$, to get

$$v^0 = \frac{6\beta\gamma}{\alpha(x_0)}. \tag{4.10}$$

Then, the solution to (4.9) with matching condition $\tilde{v}_0(x_0) = v^0$ is written as

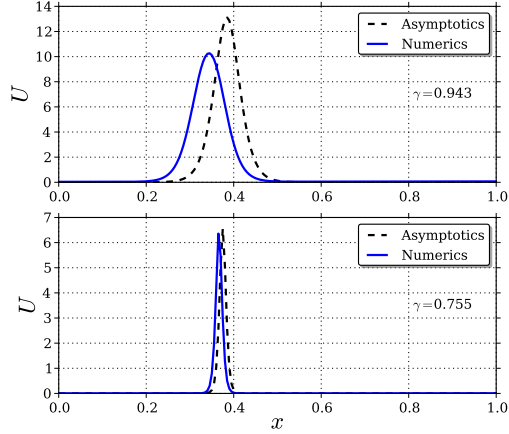$$\tilde{v}_0(x) = v^0 + G(x; x_0) - G(x_0; x_0), \tag{4.11}$$

15

Fig. 4.1: Comparison between the asymptotic and numerics of the single interior spike quasi-steady-state solution at the same location point, and parameter values given in Table 2.1(a) (top) and Table 2.1(b) (bottom).

where $G(x; x_0)$ is the unique Neumann Green's function satisfying

$$D_0 G_{xx} = -1 + \delta(x - x_0), \quad 0 < x < 1; \tag{4.12}$$

$$G_x(0; x_0) = G_x(1; x_0) = 0; \quad \int_0^1 G(x; x_0)\, dx = 0,$$

which is readily calculated analytically as

$$G(x; x_0) = -\frac{1}{2D_0}(x - x_0)^2 - \frac{1}{3D_0}\left((1 - x_0)^3 + x_0^3\right) +$$
$$+ \frac{1}{D_0}\left\{ \begin{array}{ll} -x_0(x - x_0), & 0 \le x \le x_0, \\ (1 - x_0)(x - x_0), & x_0 < x \le 1. \end{array} \right. \tag{4.13}$$

We summarise the results of the asymptotic construction of the quasi-steady-state solution in a formal proposition as follows:

Proposition 4.1. *Let $\varepsilon \ll 1$, $D = \mathcal{O}(\varepsilon^{-1})$ with $D = D_0/\varepsilon$ and $\gamma = \mathcal{O}(1)$. Then, a leading-order solution for U corresponding to a one-patch quasi-steady-state solution of (2.4) is*

$$U \sim \varepsilon^{-1} u \sim \frac{\varepsilon^{-1}}{\alpha(x_0)v^0} w\left(\varepsilon^{-1}(x - x_0)\right), \qquad w \equiv \frac{3}{2}\mathrm{sech}^2\left(\frac{\xi}{2}\right). \tag{4.14}$$

The leading-order inner solution for V, valid for $|x - x_0| = \mathcal{O}(\varepsilon)$ is

$$V \sim \varepsilon v^0, \qquad v^0 \equiv \frac{6\beta\gamma}{\alpha(x_0)}, \tag{4.15}$$

while the corresponding leading-order outer solution for V is

$$V \sim \varepsilon \tilde{v}_0(x), \qquad \tilde{v}_0(x) = v^0 + G(x; x_0) - G(x_0; x_0). \tag{4.16}$$

For the parameter values as given in Table 2.1, Fig. 4.1 shows a comparison between the quasi-steady-state solution for U, as given in Proposition 4.1, and that obtained from full numerical solutions of (2.4). Note that the parameter values in Table 2.1(b) have a smaller ε than those in Table 2.1(a), which allows for a more favourable comparison between the asymptotic theory and full numerical results.

4.1.2. Slow Patch Motion and the Steady-State Solution. Next, we extend the analysis to derive an ODE for the slow-time evolution of the patch location x_0, which has speed $\mathcal{O}(\varepsilon^2)$. To do so, we substitute $v_0 = v^0$ and $u_0 = w/\left[\alpha(x_0)v^0\right]$ into (4.4a), and write the resulting problem for u_1 on $-\infty < \xi < \infty$ in terms of a self-adjoint operator $\mathcal{L}_0$ as

$$\mathcal{L}_0 u_1 = -\frac{v_1}{\alpha(x_0)\left[v^0\right]^2}w^2 - \frac{\alpha'(x_0)\xi}{v^0\left[\alpha(x_0)\right]^2}w^2 - \frac{w_\xi}{\alpha(x_0)v^0}\frac{dx_0}{d\eta}\,; \tag{4.17}$$

$$\mathcal{L}_0\phi \equiv \phi_{\xi\xi} + 2w\phi - \phi\,.$$

Here v_1 satisfies (4.4b).

Since $\mathcal{L}_0 w_\xi = 0$, the solvability condition for (4.17), as derived by first multiplying (4.17) by w_ξ and then integrating the resulting expression by parts, is that

$$\frac{dx_0}{d\eta}\int_{-\infty}^{\infty}(w_\xi)^2\,d\xi = -\frac{1}{3v^0}\int_{-\infty}^{\infty}v_1\left(w^3\right)_\xi\,d\xi - \frac{\alpha'(x_0)}{3\alpha(x_0)}\int_{-\infty}^{\infty}\xi\left(w^3\right)_\xi\,d\xi\,, \tag{4.18}$$

where v^0 is given in (4.15). Upon integrating the right-hand side of (4.18) by parts, and using the fact that $w(\xi)$ is even and that $\int_{-\infty}^{\infty}w^3\,d\xi = 6\int_{-\infty}^{\infty}(w_\xi)^2\,d\xi$, we derive

$$\frac{dx_0}{d\eta} = \frac{\alpha(x_0)}{6\beta\gamma}\left[v_{1\xi}(\infty) + v_{1\xi}(-\infty)\right] + \frac{2\alpha'(x_0)}{\alpha(x_0)}\,. \tag{4.19}$$

The final step in the derivation of the patch dynamics is to enforce the matching condition between the inner and outer approximations for v that $v_{1\xi}(\pm\infty) = \tilde{v}_{0x}(x_0^\pm)$. From $D_0\left(v_{1\xi}(\infty) - v_{1\xi}(-\infty)\right) = 1$, which comes from integrating (4.4b) across the real line, and (4.11), this yields that $v_{1\xi}(\pm\infty) = G_x(x_0^\pm;x_0)$. Consequently, (4.19) becomes

$$\frac{dx_0}{d\eta} = \frac{\alpha(x_0)}{6\beta\gamma}\left(G_x(x_0^+;x_0) + G_x(x_0^-;x_0)\right) + \frac{2\alpha'(x_0)}{\alpha(x_0)}\,,$$

where $G_x(x_0^\pm;x_0)$ can be calculated from (4.13). We summarise our result for the slow dynamics of a single patch in a formal proposition as follows:

Proposition 4.2. *Let $\varepsilon \ll 1$, $D = \mathcal{O}(\varepsilon^{-1})$ with $D = D_0/\varepsilon$ and $\gamma = \mathcal{O}(1)$. Then, the slow dynamics of a single-patch quasi-steady-state solution of (2.4) on the time-scale $\eta = \varepsilon^2 t$ is given to leading order by*

$$U \sim \varepsilon^{-1}u(\eta,x)\,, \qquad u(\eta,x) \sim \frac{3}{2\alpha(x_0)v^0}\mathrm{sech}^2\left(\frac{\varepsilon^{-1}}{2}(x - x_0)\right)\,,$$

$$\tag{4.20}$$

$$V \sim \varepsilon v(\eta,x)\,, \qquad v(\eta,x) \sim v^0 + G(x;x_0) - G(x_0;x_0)\,, \qquad v^0 = \frac{6\beta\gamma}{\alpha(x_0)}\,,$$

where the slow dynamics of the patch location $x_0(\eta)$ satisfies the ODE

$$\frac{dx_0}{d\eta} = \frac{\alpha(x_0)}{3\beta\gamma D_0}\left(\frac{1}{2} - x_0\right) + \frac{2\alpha'(x_0)}{\alpha(x_0)}\,. \tag{4.21}$$

A steady-state one-patch solution is located at a point x_0^* with $0 < x_0^* < 1$, for which $dx_0/d\eta = 0$. Thus, from (4.21), any equilibrium point must be a root of $\mathcal{G}(x_0)$, where $\mathcal{G}(x_0)$ is defined by

$$\mathcal{G}(x_0) \equiv \frac{1}{6\beta\gamma D_0}\left(\frac{1}{2} - x_0\right) + \frac{\alpha'(x_0)}{\alpha(x_0)^2}\,.$$
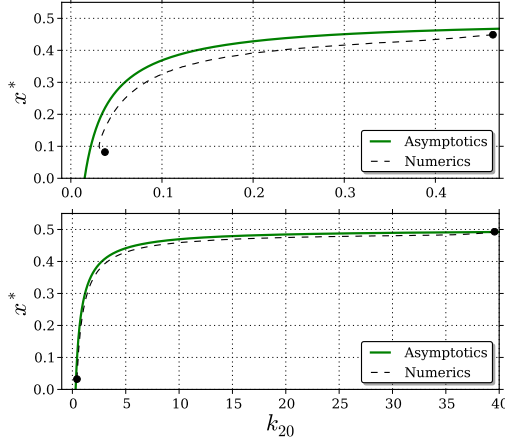
Fig. 4.2: Comparison between the asymptotic formula (4.23) and numerical continuation results for the equilibrium patch location x_0^* while varying the parameter k_{20}. The other parameter values as given in Table 2.1(a) (top) and Table 2.1(b) (bottom). Solid dots represent fold bifurcation points of the numerical solutions.

For the case of interest where $\alpha(x_0) > 0$ for all $x_0 \in [0, 1]$ and $\alpha'(x_0) < 0$ for all $x_0 \in (0, 1)$, we conclude that $\mathcal{G}(x_0) < 0$ on $1/2 \le x_0 < 1$. Therefore, any root to $\mathcal{G}(x_0) = 0$ must satisfy $0 < x_0 < 1/2$. Next, we calculate that $\mathcal{G}(0) > 0$ when

$$-\frac{\alpha'(0)}{[\alpha(0)]^2} < \frac{1}{12\beta\gamma D_0}\,, \tag{4.22a}$$

and, furthermore, $\mathcal{G}'(x_0) < 0$ when

$$\frac{\alpha''(x_0)}{[\alpha(x_0)]^2} - 2\frac{[\alpha'(x_0)]^2}{[\alpha(x_0)]^3} < \frac{1}{6\beta\gamma D_0}\,. \tag{4.22b}$$

If (4.22) hold, then the slow dynamics (4.21) admits a unique stable equilibrium solution x_0^* in $0 < x_0^* < 1/2$, which corresponds to a unique and stable equilibrium patch location with respect to the slow dynamics. We summarise this result in a formal proposition as follows:

Proposition 4.3. *Suppose that $\alpha(x_0) > 0$ for all $x_0 \in [0, 1]$ and $\alpha'(x_0) < 0$ for all $x_0 \in (0, 1)$, and that (4.22) hold. Then, the slow dynamics (4.21) has a unique stable equilibrium solution x_0^* in $0 < x_0^* < 1/2$. The resulting equilibrium solution is given asymptotically by (4.20) with $x_0 = x_0^*$.*

For the choice of spatial gradient $\alpha(x_0) = \exp(-\nu x_0)$ where $\nu > 0$, which was used in our numerical computations in §3, the condition (4.22b) is automatically satisfied, whereas (4.22a) holds when $\nu < (12\beta\gamma D_0)^{-1}$. Under this constraint on ν, a patch will drift slowly on an $\mathcal{O}\left(\varepsilon^{-2}\right)$ time-scale to be eventually pinned to a location x_0^* on the half-interval $0 < x_0^* < 1/2$.

In terms of the original parameters, the equilibrium point x_0^* can be then written implicitly as $k_{20} = k_{20}\left(x_0^*\right)$ where

$$k_{20}\left(x_0^*\right) = \frac{6\nu r D_2 \sqrt{D_1(c + r)}}{b^2 L^2} \frac{\left(\alpha\left(x_0^*/L\right)\right)^{-1}}{L/2 - x_0^*}\,, \qquad 0 \le x_0 \le L\,. \tag{4.23}$$

Fig. 4.2 shows a comparison between full numerical results and our asymptotic results for the equilibrium location of a single patch as a function of k_{20} for the parameter values in Table 2.1. The full numerical

result for the single-patch location is given by the solid curve, and our asymptotic result of (4.23) is given by the dashed curve. This figure shows that there is a rather close agreement between the asymptotic and numerical results provided that k_{20} is not too small nor too large because the asymptotic analysis is unable to predict the numerically observed fold bifurcations. Note that this is consistent with the asymptotics breaking down if x_0 or $(x_0 - 1/2)$ become $\mathcal{O}(\varepsilon)$. It is clear that the asymptotics must break down as $x_0 \to 0$ because it is assumed that x_0 is $O(1)$. In the limit $x_0 \to 1/2$, we find that the first term in ODE (4.21) becomes $O(\varepsilon)$ and additional terms would need to be included to accurately predict a fold bifurcation.

4.2. Boundary Patch Solution. As can be noted from the bifurcation diagram in Fig. 3.1, the patch pinned to the left-hand boundary at $x = 0$ is a quasi-steady solution, so we can also readily construct a half-patch equilibrium solution. Since the details of the analysis are similar to that in §4.1.1 we only briefly outline the calculation.

In the inner region near $x = 0$, we obtain to leading-order that

$$v \sim v_b^0, \qquad u \sim u_0 = \frac{1}{\alpha(0)v_b^0} w\left(\frac{x}{\varepsilon}\right), \qquad w(\xi) = \frac{3}{2}\text{sech}^2\left(\frac{\xi}{2}\right), \tag{4.24}$$

where v_b^0 is an unknown constant, representing the leading-order inner solution for v.

In the outer region, $\mathcal{O}(\varepsilon) \ll x \le 1$, the leading-order outer solution $\tilde{v}_0$ for v satisfies

$$D_0\tilde{v}_{0xx} = -1, \quad 0 < x < 1; \qquad \tilde{v}_{0x}(1) = 0, \qquad \tilde{v}_{0x}(0^+) = \frac{3\beta\gamma}{\alpha(0)v_b^0 D_0}, \tag{4.25}$$

with the matching condition that $\lim_{x\to 0} \tilde{v}_0(x) = v_b^0$. Upon integrating (4.25) over the domain, we obtain the solvability condition that $v_b^0 = 3\beta\gamma/\alpha(0)$. Then, the solution to (4.25) can be written as

$$\tilde{v}_0 = v_b^0 + G_b(x) - G_b(0), \tag{4.26}$$

where $G_b(x)$ is the Neumann Green's function satisfying

$$D_0 G_{bxx} = -1, \quad 0 < x < 1; \tag{4.27}$$

$$G_{bx}(1) = 0, \quad D_0 G_{bx}(0^+) = 1; \quad \int_0^1 G_b(x)\, dx = 0,$$

which has the explicit solution

$$G_b(x) = -\frac{1}{2D_0}x^2 + \frac{x}{D_0} - \frac{1}{3D_0}. \tag{4.28}$$

We summarise the result in a formal proposition as follows:

Proposition 4.4. *Let $\varepsilon \ll 1$, $D = \mathcal{O}(\varepsilon^{-1})$ with $D = D_0/\varepsilon$ and $\gamma \sim \mathcal{O}(1)$. Then, a single boundary patch solution to (2.4) centred on the boundary $x = 0$ is given asymptotically by*

$$U \sim \frac{3\varepsilon^{-1}}{2\alpha(0)v_b^0}\text{sech}^2\left(\frac{x}{2\varepsilon}\right), \qquad V \sim \varepsilon^{-1}\left(v_b^0 + \frac{1}{D_0}x\left(1 - \frac{x}{2}\right)\right), \qquad v_b^0 = \frac{3\beta\gamma}{\alpha(0)}. \tag{4.29}$$

Fig. 4.3 shows a favourable comparison between full numerical results for U and the corresponding asymptotic result for U given in Proposition 4.4.
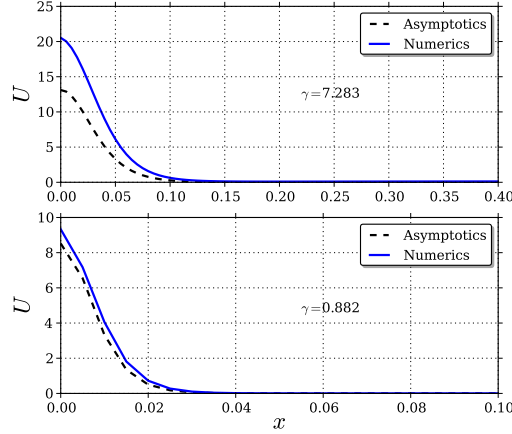
Fig. 4.3: Comparison between the numerical solution and the asymptotic quasi-steady-state solution, as derived in Proposition 4.4, for parameter values in Table 2.1(a) (top) and Table 2.1(b) (bottom).

4.3. Multiple Patch Solution. A similar asymptotic approach can be used to characterise multiple patch (or spike) solutions. We will consider the case of $N+1$ interior patches for which no patches are $\mathcal{O}(\varepsilon)$ close to each other or to either boundary. We first construct a quasi-steady-state solution with patches at locations $x_0, \ldots, x_N$ with $x_i < x_j$ for $i < j$. We then derive an ODE system characterising the slow dynamics of this quasi-steady-state multi-patch solution.

By proceeding as in §4.1.1, the leading-order outer solution $\tilde{v}_0$ for v satisfies

$$D_0 \tilde{v}_{0xx} = -1 + \sum_{i=0}^{N} n_i \delta(x - x_i), \quad 0 < x < 1; \tag{4.30}$$

$$\tilde{v}_{0x}(0) = \tilde{v}_{0x}(1) = 0; \quad n_i \equiv \frac{6\beta\gamma}{\alpha(x_i) v^i}.$$

The $N+1$ matching conditions are that $\tilde{v}_0(x_i) = v^i$, where v^i is the leading-order approximation for v in the inner region near the i-th patch. The solvability condition for (4.30) is that $\sum_{i=0}^{N} n_i = 1$.

The solution to (4.30) can be written in terms of the Neumann Green's function of (4.12) as

$$\tilde{v}_0(x) = \bar{v}_0 + \sum_{j=0}^{N} G(x; x_j) n_j, \tag{4.31}$$

where $\bar{v}_0$ is an unknown constant. The $N+1$ matching conditions $\tilde{v}_0(x_i) = v^i$, together with $\sum_{i=0}^{N} n_i = 1$, give a linear system of $N+2$ equations for the unknowns v^i for $i = 0, \ldots, N$ and $\bar{v}_0$ as

$$v^i = \sum_{j=0}^{N} G_{ij} n_j + \bar{v}_0, \quad i = 0, \ldots, N; \qquad \sum_{j=0}^{N} n_j = 1; \qquad G_{ij} \equiv G(x_i; x_j). \tag{4.32}$$

The system (4.32) is written in matrix form by introducing the vectors

$$\mathbf{e} \equiv (1, \ldots, 1)^T, \quad \mathbf{n} \equiv (n_0, \ldots, n_N)^T, \quad \mathbf{n}_{-1} \equiv (1/n_0, \ldots, 1/n_N)^T,$$

where ^{T} denotes transpose. Then, (4.32) becomes

$$6\beta\gamma \mathbf{B}\mathbf{n}_{-1} = \mathbf{G}\mathbf{n} + \bar{v}_0 \mathbf{e}, \qquad \mathbf{n}^T \mathbf{e} = 1. \tag{4.33}$$

20

Here the symmetric Green's matrix $\mathbf{G}$ and the diagonal matrix $\mathbf{B}$ are defined by

$$\mathbf{G} \equiv \begin{pmatrix} G_{00} & G_{01} & \cdots & G_{0N} \\ G_{10} & \ddots & & G_{1N} \\ \vdots & & \ddots & \vdots \\ G_{N0} & \cdots & G_{NN-1} & G_{NN} \end{pmatrix}, \quad \mathbf{B} \equiv \begin{pmatrix} 1/\alpha(x_0) & 0 & \cdots & 0 \\ 0 & \ddots & & 0 \\ \vdots & & \ddots & \vdots \\ 0 & \cdots & 0 & 1/\alpha(x_N) \end{pmatrix}.$$

The constant $\bar{v}_0$ is obtained by taking the dot product of the first equation in (4.33) with $\mathbf{n}$ and using $\mathbf{n}^T \mathbf{e} = 1$. This yields

$$\bar{v}_0 = 6\beta\gamma(N+1)\bar{\alpha}_{-1} - \mathbf{n}^T \mathbf{G}\mathbf{n}; \quad \bar{\alpha}_{-1} \equiv \frac{1}{N+1}\left(\frac{1}{\alpha(x_0)} + \cdots + \frac{1}{\alpha(x_N)}\right). \tag{4.34}$$

By using this expression for $\bar{v}_0$ in (4.33), we obtain a nonlinear algebraic system for $\mathbf{n}$. The construction of the quasi-equilibrium solution is summarized in a formal proposition as follows:

Proposition 4.5. *Let $\varepsilon \ll 1$, $D = \mathcal{O}(\varepsilon^{-1})$ with $D = D_0/\varepsilon$ and $\gamma = \mathcal{O}(1)$, and consider an $N+1$ interior patch quasi-steady state solution of (2.4) with patches centred at $x_0, \ldots, x_N$. Then, a leading order approximation for U and V is*

$$U \sim \frac{\varepsilon^{-1}}{6\beta\gamma} \sum_{j=0}^{N} w\left(\varepsilon^{-1}(x - x_j)\right) n_j, \tag{4.35a}$$

$$V \sim \varepsilon\left(6\beta\gamma(N+1)\bar{\alpha}_{-1} - \mathbf{n}^T \mathbf{G}\mathbf{n} + \sum_{j=0}^{N} G(x; x_j) n_j\right), \tag{4.35b}$$

where $w(\xi) = \frac{3}{2}\mathrm{sech}^2(\xi/2)$, $G(x; x_j)$ satisfies (4.12), and $\bar{\alpha}_{-1}$ is defined in (4.34). Here $\mathbf{n} = (n_0, \ldots, n_N)^T$ is the solution to the nonlinear algebraic system

$$6\beta\gamma\mathbf{B}\mathbf{n}_{-1} = \mathbf{G}\mathbf{n} + 6\beta\gamma(N+1)\bar{\alpha}_{-1}\mathbf{e} - \left(\mathbf{n}^T \mathbf{G}\mathbf{n}\right)\mathbf{e}. \tag{4.36}$$

In terms of n_i, the leading-order solution for V in the vicinity of the i-th patch is $V^i \sim 6\varepsilon\beta\gamma/\alpha(x_i)n_i$.

Next, to characterise the slow dynamics of the collection of patches, we introduce the slow time scale $\eta = \varepsilon^2 t$ and we let the patch locations evolve slowly in time as $x_j = x_j(\eta)$ for $j = 0, \ldots, N$. Upon proceeding as in §4.1.2, we obtain for the j-th patch that

$$\frac{dx_j}{d\eta} = \frac{\alpha(x_j)n_j}{6\beta\gamma}\left(\tilde{v}_{0x}(x_j^+) + \tilde{v}_{0x}(x_j^-)\right) + \frac{2\alpha'(x_j)}{\alpha(x_j)}, \quad j = 0, \ldots, N. \tag{4.37}$$

By using (4.31) for $\tilde{v}_0$, we can express this result in terms of the Green's function. The slow dynamics is summarised in the following formal proposition:

Proposition 4.6. *Under the assumptions of Proposition 4.5, the slow dynamics on a time scale $\eta = \varepsilon^2 t$ of a collection of $N+1$ interior patches satisfies the differential algebraic (DAE) system consisting of the ODE's*

$$\frac{dx_j}{d\eta} = \frac{\alpha(x_j)n_j}{3\beta\gamma}\left(\langle G_x\rangle_j n_j + \sum_{i\neq j}^{N} G_x(x_j; x_i) n_i\right) + \frac{2\alpha'(x_j)}{\alpha(x_j)}, \quad j = 0, \ldots, N, \tag{4.38}$$

coupled to the nonlinear algebraic system (4.36). In (4.38), we have defined

$$\langle G_x\rangle_j \equiv \frac{1}{2}\left(G_x(x_j^+; x_j) + G_x(x_j^-; x_j)\right).$$

It is analytically cumbersome to investigate in full generality the solvability of the DAE system for finding quasi-steady solutions for $N+1$ patches and to analyse the slow dynamics and equilibrium positions for such solutions. To illustrate our result we will only consider two-patch quasi-steady-state solutions.

First, consider the two-interior patch case with patches at x_0 and x_1 where $0 < x_0 < x_1 < 1$. Then, the nonlinear algebraic system (4.36) reduces to

$$\frac{6\beta\gamma}{\alpha(x_0)n_0} = G_{00}n_0 + G_{01}n_1 + \frac{6\beta\gamma}{\alpha(x_0)} + \frac{6\beta\gamma}{\alpha(x_1)} - \left[G_{00}n_0^2 + 2G_{10}n_0n_1 + G_{11}n_1^2\right],$$

$$\frac{6\beta\gamma}{\alpha(x_1)n_1} = G_{10}n_0 + G_{11}n_1 + \frac{6\beta\gamma}{\alpha(x_0)} + \frac{6\beta\gamma}{\alpha(x_1)} - \left[G_{00}n_0^2 + 2G_{10}n_0n_1 + G_{11}n_1^2\right],$$

where $G_{01} = G_{10}$ by the reciprocity of the Green's function. By subtracting these equations, and then using $n_1 = 1 - n_0$, we obtain a scalar nonlinear algebraic equation for n_0 given by

$$6\beta\gamma\left[\frac{1}{\alpha(x_0)n_0} - \frac{1}{\alpha(x_1)(1-n_0)}\right] = (G_{00} - 2G_{01} + G_{11})n_0 + G_{01} - G_{11}.$$

By using the explicit result for $G(x;x_0)$ given in (4.13), we calculate that

$$G_{01} - G_{11} = \frac{1}{2D_0}\left(x_1^2 - x_0^2\right), \qquad G_{00} - 2G_{01} + G_{11} = \frac{1}{D_0}\left(x_0 - x_1\right).$$

Similarly, the two ODE's in (4.38) for x_0 and x_1 can be written explicitly by using (4.13) to calculate the required gradients of the Green's function. We readily evaluate that

$$G_x(x_1;x_0) = \frac{1}{D_0}(1 - x_1), \quad G_x(x_0;x_1) = -\frac{1}{D_0}x_0, \quad \langle G_x\rangle_j = \frac{1}{D_0}\left(\frac{1}{2} - x_j\right),$$

for $j = 0, 1$. Upon taking into account that $n_1 = 1 - n_0$ in (4.38), we obtain the following explicit DAE system for the evolution of two interior patches:

Proposition 4.7. *Under the conditions of Proposition 4.5, the slow dynamics of a quasi-steady-state solution with two interior patches is characterised by the DAE system*

$$\frac{dx_0}{d\eta} = \frac{n_0}{3\beta\gamma D_0}\alpha(x_0)\left(\frac{n_0}{2} - x_0\right) + \frac{2\alpha'(x_0)}{\alpha(x_0)}, \tag{4.39a}$$

$$\frac{dx_1}{d\eta} = \frac{1 - n_0}{3\beta\gamma D_0}\alpha(x_1)\left(\frac{1 + n_0}{2} - x_1\right) + \frac{2\alpha'(x_1)}{\alpha(x_1)}, \tag{4.39b}$$

where $n_0 = n_0(x_0, x_1)$ with $0 < n_0 < 1$, is a root of the nonlinear algebraic equation

$$\mathcal{F}(n_0) = \mathcal{H}(n_0), \tag{4.40}$$

$$\mathcal{F}(n_0) \equiv 6\beta\gamma\left(\frac{1}{\alpha(x_0)n_0} - \frac{1}{\alpha(x_1)(1-n_0)}\right), \qquad \mathcal{H}(n_0) \equiv mn_0 + p,$$

in which $m \equiv (x_0 - x_1)/D_0 < 0$ and $p \equiv \left(x_1^2 - x_0^2\right)/2D_0 > 0$.

We now investigate the solvability of the nonlinear algebraic equation (4.40). Since $\mathcal{F}(n_0)$ tends to infinity as $n_0 \longrightarrow 0^+$ and $\mathcal{F}(n_0) \longrightarrow -\infty$ as $n_0 \longrightarrow 1^-$, it follows that there must be at least one root n_0^* to (4.40) for $0 < n_0^* < 1$. However, non-uniqueness of solutions can not be ruled out as $x_0 < x_1$, which would be require $m < 0$. Numerically we find that this root is unique for $\gamma > 0.085$ for the parameter values in Table 2.1(b).
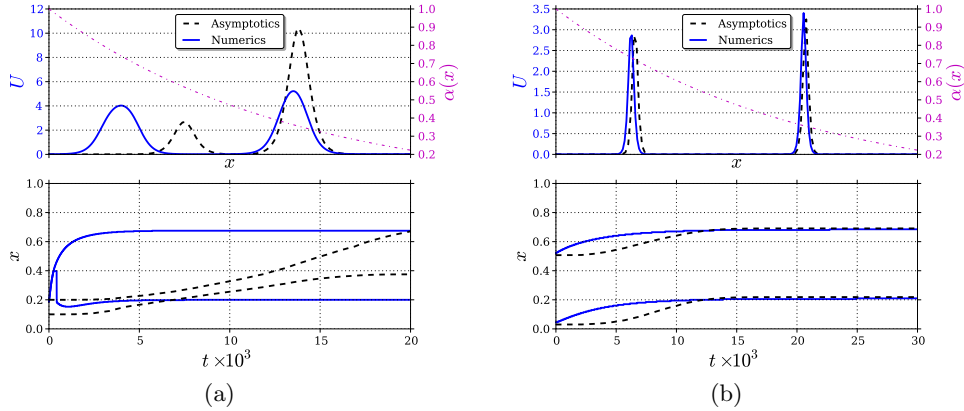
Fig. 4.4: Profile (top) and time-dependent spike locations (bottom) for the two interior spikes case. DAE system (4.39) is solved numerically, and the quasi-steady-state solution is compared to full numerics where n_0 is computed from (4.40). Notice that the spike that is closer to the boundary $x = 0$ has lower amplitude. This is a consequence of decreasing gradient (represented by the dot-dash line in the upper plot), as can be seen from formulas (4.30) for n_j and quasi-steady-state solution (4.35) for U. (a) Here $\gamma = 0.1222$, $n_0 = 0.3687$ and other parameter values as given in Table 2.1(a). (b) Here $\gamma = 0.1182$, $n_0 = 0.4942$ and other parameter values as given in Table 2.1(b).

Fig. 4.4(b) shows a favourable comparison between full numerical results for U and the corresponding asymptotic result for U given in Proposition 4.5 and Proposition 4.7 for the two-interior-spikes case. However, notice there is no favourable comparison, in Fig. 4.4(a), for parameter set as given in Table 2.1(a) presumably due to the fact that this is effectively a smaller domain and finite size effects are more pronounced when trying to fit more than one pulse.

4.3.1. Boundary and Interior Patch Solution. Next, we construct a quasi-steady-state solution for (2.4) that has a boundary patch at $x = 0$ and an interior patch at $x = x_1$. The slow dynamics of the interior patch is also determined. Since the analysis is similar to the one above we will only briefly outline the derivation.

A leading-order uniformly valid approximation for the quasi steady-state solution for u is

$$u \sim \frac{1}{\alpha(0)v^0} w\left(\frac{x}{\varepsilon}\right) + \frac{1}{\alpha(x_1)v^1} w\left(\frac{x - x_1}{\varepsilon}\right).$$

(4.41)

In the inner regions, $v \sim v^0$ in $x = \mathcal{O}(\varepsilon)$ and $v \sim v^1$ in $|x - x_1| = \mathcal{O}(\varepsilon)$, where v^0 and v^1 are constants to be found.

In place of (4.30), the leading-order solution $\tilde{v}_0$ for the outer approximation of v satisfies

$$D_0 \tilde{v}_{0xx} = -1 + \frac{6\beta\gamma}{\alpha(x_1)v^1}\delta(x - x_1), \quad 0 < x < 1;$$

(4.42)

$$\tilde{v}_{0x}(1) = 0, \quad D_0\tilde{v}_{0x}\left(0^+\right) = \frac{3\beta\gamma}{\alpha(0)v^0},$$

subject to the two matching conditions that $\tilde{v}_0(0) = v^0$ and $\tilde{v}_0(x_1) = v^1$. By integrating the equation for $\tilde{v}_0$ over the domain, we derive that

$$\frac{n_0}{2} + n_1 = 1; \quad \text{where} \quad n_0 \equiv \frac{6\beta\gamma}{\alpha(0)v^0}, \quad n_1 \equiv \frac{6\beta\gamma}{\alpha(x_1)v^1}.$$

(4.43)

23

The solution to (4.42) is

$$\tilde{v}_0(x) = n_1 G(x; x_1) + \frac{n_0}{2} G_b(x) + \bar{v}_0 \,, \tag{4.44}$$

where $G(x; x_1)$ and $G_b(x)$ are the Green's functions of (4.12) and (4.27). Here $\bar{v}_0$ is again to be determined. By imposing $\tilde{v}_0(0) = v^0$ and $\tilde{v}_0(x_1) = v^1$, we obtain that n_0 and n_1 satisfy the coupled system

$$\frac{6\beta\gamma}{\alpha(0)n_0} = n_1 G(0; x_1) + \frac{n_0}{2} G_b(0) + \bar{v}_0 \,, \qquad \frac{6\beta\gamma}{\alpha(x_1)n_1} = n_1 G(x_1; x_1) + \frac{n_0}{2} G_b(x_1) + \bar{v}_0 \,.$$

By subtracting these two equations, and by using $n_0 = 2(1 - n_1)$, we get that n_1 satisfies the scalar nonlinear algebraic equation

$$6\beta\gamma \left(\frac{1}{\alpha(x_1)n_1} - \frac{1}{2(1 - n_1)\alpha(0)} \right) = mn_1 + p \,, \tag{4.45}$$

where $m \equiv G(x_1; x_1) - G(0; x_1) - G_b(x_1) + G_b(0)$ and $p \equiv G_b(x_1) - G_b(0)$. Then, by using (4.13) and (4.28) for the two Green's functions, m and p can be evaluated explicitly. The result is given below in (4.48).

With regards to the dynamics of the interior patch, the result (4.37) still applies, but where $\tilde{v}_0$ in (4.37) is now given by (4.44). In this way, we get

$$\frac{dx_1}{d\eta} = \frac{\alpha(x_1)n_1}{3\beta\gamma} \left(n_1 \langle G_x \rangle_1 + \frac{n_0}{2} G_{bx}(x_1) \right) + \frac{2\alpha'(x_1)}{\alpha(x_1)} \,. \tag{4.46}$$

Then, by using (4.13) and (4.28), together with $n_0 = 2(1 - n_1)$, we can explicitly calculate the terms in this ODE involving the Green's functions. The result is summarised in the following formal proposition:

Proposition 4.8. *Under the conditions of Proposition 4.5, the slow dynamics of a quasi-steady-state solution with a boundary patch at $x = 0$ and an interior patch at $x = x_1$ is characterised by the DAE system*

$$\frac{dx_1}{d\eta} = \frac{n_1}{3\beta\gamma D_0} \alpha(x_1) \left(1 - \frac{n_1}{2} - x_1 \right) + \frac{2\alpha'(x_1)}{\alpha(x_1)} \,, \tag{4.47}$$

where $0 < n_1 < 1$, which depends on x_1, is a root of the nonlinear algebraic equation

$$\mathcal{F}_b(n_1) = \mathcal{H}_b(n_1) \,; \tag{4.48}$$

$$\mathcal{F}_b(n_1) \equiv 6\beta\gamma \left(\frac{1}{\alpha(x_1)n_1} - \frac{1}{2(1 - n_1)\alpha(0)} \right) \,, \quad \mathcal{H}_b(n_1) \equiv mn_1 + p \,,$$

in which $m \equiv -x_1/D_0 < 0$ and $p \equiv x_1 (1 - x_1/2)/D_0 > 0$.

Since $\mathcal{F}_b(n_1) \longrightarrow \infty$ as $n_1 \longrightarrow 0^+$ and $\mathcal{F}_b(n_1) \longrightarrow -\infty$ as $n_1 \longrightarrow 1^-$, it follows that there must be a root n_1^* to (4.40) on $0 < n_1^* < 1$. However, as in Proposition 4.7, solution uniqueness can not be guaranteed as $m < 0$.

5. Competition Instability of Multi-Patch Patterns. In §3 a numerical bifurcation analysis was used to determine the effect on the solution of changing both the auxin rate parameter k_{20} and the length of the domain. While the trends of the asymptotic analysis are similar to the numerical bifurcation diagrams, the slow-time asymptotics of §4 has not been able to capture fold bifurcations in the correct parameters. In this section, using a different method, we derive a sufficient condition for which a multi-patch pattern can become unstable to an $\mathcal{O}(1)$ time-scale instability as either k_{20} or the length of the domain is varied. Such
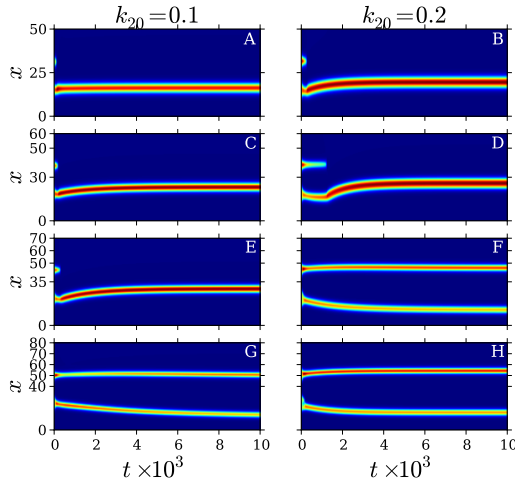
Fig. 5.1: A single-patch and two-patch outcome for several lengths and two k_{20} values; using the parameter set given in Table 2.1(a), the k_{20}-values indicated and (A)-(B) $L = 50$, (C)-(D) $L = 60$, (E)-(F) $L = 70$, (G)-(H) $L = 80$.

an instability occurs on a time scale much faster than that of the slow dynamics of the patches studied in §4.1.2.

In terms of the original variables of (2.4), we first illustrate this instability by considering two-patch solutions on a domain of length L for various k_{20} values. From full numerical solutions of (2.4), starting with an initial condition of a two-patch steady-state solution, in Fig. 5.1 below we show the eventual fate of a two-patch solution as t increases for either $L = 50, 60, 70, 80$ and for either $k_{20} = 0.1, 0.2$. The results for $k_{20} = 0.1$ for the four different values of L are shown in the first column of Fig. 5.1. There we observe that the two-patch pattern is destroyed rather quickly for $L = 50, 60, 70$ (frames A,C,E), and it persists only when $L = 80$ (frame G). However, if we increase the value of k_{20} up to $k_{20} = 0.2$, then as shown in the second column of Fig. 5.1, the two-patch pattern is annihilated suddenly only when $L = 50, 60$ (frame B, D). Based on these numerical results, we might conjecture that an $\mathcal{O}(1)$ time-scale instability is triggered for a multi-patch pattern when the domain length is below some threshold, and that this threshold value depends on k_{20}. This type of instability, leading to the destruction of some patches in a multi-patch pattern, has been previously called a competition instability in the context of the Gierer–Meinhardt model [22] and other systems, see [23, 50], for instance.

5.1. A Non-local Eigenvalue Problem. The analysis of this $\mathcal{O}(1)$ time-scale instability is based upon first linearising (2.4) around the quasi-steady-state solution, denoted here by u_s and v_s, as given asymptotically in Proposition 4.5. In the linearization we "freeze" the locations of the patches, since they evolve only on an $\mathcal{O}\left(\varepsilon^{-2}\right)$ time-scale that is very long in comparison with the fast $\mathcal{O}(1)$ time-scale instability that we are seeking. After performing an asymptotic reduction of this linearised problem, we obtain a non-local eigenvalue problem whose spectrum governs the competition instability. The eigenvalue problem is obtained by substituting

$$u(t,x) = u_s + e^{\lambda t}\varphi(x), \quad v(t,x) = v_s + e^{\lambda t}\psi(x), \qquad \varphi, \psi \ll 1, \tag{5.1}$$

25

into (2.4) to obtain, on $0 < x < 1$, that

$$\varepsilon^2 \varphi_{xx} - \varphi + 2\alpha(x)u_s v_s \varphi + \alpha(x)u_s^2 \psi + \frac{\varepsilon^2}{\tau\gamma}\psi = \lambda\varphi\,, \tag{5.2a}$$

$$D_0\psi_{xx} - \varepsilon^{-1}\tau\gamma\alpha(x)u_s^2\psi - \varepsilon\psi = \varepsilon^{-1}\left(\tau\gamma\left(2\alpha(x)u_s v_s \varphi - \varphi\right) + \beta\gamma\varphi\right) + \varepsilon\tau\lambda\psi\,, \tag{5.2b}$$

where $\phi_x = \psi_x = 0$ at $x = 0, 1$.

As similar to [23], the eigenfunction for the fast component is localized and has the form

$$\varphi(x) \sim \sum_{j=0}^{N} \varphi_j\left(\varepsilon^{-1}\left(x - x_j\right)\right)\,, \qquad \varphi_j \longrightarrow 0 \qquad \text{as} \qquad |\xi| \longrightarrow \infty\,.$$

By substituting this form into (5.2a), and using the leading-order inner results $u_s \sim w/\left[\alpha(x_j)v^j\right]$ and $v_s \sim v^j \sim 6\beta\gamma/\alpha(x_j)n_j$, as given in Proposition 4.5, we conclude that φ_j satisfies

$$\mathcal{L}_0\varphi_j + \frac{n_j^2}{36\beta^2\gamma^2}\alpha\left(x_j\right)w^2\psi\left(x_j\right) = \lambda\varphi_j\,, \quad -\infty < \xi < \infty\,, \tag{5.3}$$

with $\varphi_j \longrightarrow$ as $|\xi| \longrightarrow \infty$, where $\mathcal{L}_0\varphi \equiv \varphi_{\xi\xi} + 2w\varphi - \varphi$ is the local operator of linearization around the spike solution w given by (4.5). Key properties of the eigenvalue problem for $\mathcal{L}_0$ are given in Theorem 2.5 of [51]). Here n_j is to be computed from the nonlinear algebraic system in (4.36).

In order to determine $\psi(x_j)$ in (5.3) we must formulate an outer problem for ψ from (5.2b) that is valid except at $\mathcal{O}(\varepsilon)$ distances from the patch locations. To do so, we use the fact that, since u_s is localized near each patch, the $\mathcal{O}\left(\varepsilon^{-1}\right)$ terms in (5.2b) can be approximated for $\varepsilon \ll 1$ as Dirac masses

$$\varepsilon^{-1}\tau\gamma\alpha(x)u_s^2\psi \longrightarrow \frac{\tau}{36\beta^2\gamma}\left(\int_{-\infty}^{\infty} w^2\,d\xi\right)\sum_{j=0}^{N} n_j^2\alpha\left(x_j\right)\psi\,\delta\left(x - x_j\right)\,,$$

$$\varepsilon^{-1}\left(\tau\gamma\left(2\alpha(x)u_s v_s \varphi - \varphi\right) + \beta\gamma\varphi\right) \longrightarrow 2\tau\gamma\sum_{j=0}^{N}\int_{-\infty}^{\infty}\left(w - \frac{1}{2}\left(1 - \frac{\beta}{\tau}\right)\right)\varphi_j\,d\xi\,\delta\left(x - x_j\right)\,.$$

Upon substituting these formulae into (5.2b), we obtain in the outer region that ψ satisfies

$$D_0\psi_{xx} - \frac{\tau}{6\beta^2\gamma}\left(\sum_{j=0}^{N} n_j^2\alpha\left(x_j\right)\delta\left(x - x_j\right)\right)\psi = 2\tau\gamma\sum_{j=0}^{N}\delta\left(x - x_j\right)\int_{-\infty}^{\infty}\left(w - \frac{1}{2}\left(1 - \frac{\beta}{\tau}\right)\right)\varphi_j\,d\xi\,, \tag{5.4}$$

on $0 < x < 1$ subject to $\psi_x(0) = \psi_x(1) = 0$. This problem is equivalent to seeking a continuous function $\psi(x)$ satisfying

$$\psi_{xx} = 0\,, \qquad 0 < x < 1\,; \qquad \psi_x(0) = \psi_x(1) = 0\,, \tag{5.5}$$

subject to the following jump conditions on the derivative at each x_j:

$$D_0\left(\psi_x\left(x_j^+\right) - \psi_x\left(x_j^-\right)\right) = \frac{a_j}{\gamma}\psi_j + \gamma b_j\,, \qquad j = 0, \dots, N\,. \tag{5.6}$$

Here we have defined ψ_j, a_j, and b_j, for $j = 0, \dots, N$, by

$$\psi_j = \psi\left(x_j\right)\,, \quad a_j \equiv \frac{\tau n_j^2}{6\beta^2}\alpha\left(x_j\right)\,, \quad b_j \equiv 2\tau\int_{-\infty}^{\infty}\left(w - \frac{1}{2}\left(1 - \frac{\beta}{\tau}\right)\right)\varphi_j\,d\xi\,. \tag{5.7}$$

26

We now solve this problem explicitly to determine the ψ_j, which are needed in (5.3). As in [50], we define the positive semi-definite matrix $\mathbf{N}$ by

$$\mathbf{N} \equiv \begin{pmatrix} l_1 & -l_1 & 0 & \cdots & 0 & 0 & 0 \\ -l_1 & l_1 + l_2 & l_2 & \ddots & \ddots & 0 & 0 \\ 0 & \ddots & \ddots & \ddots & \ddots & \ddots & 0 \\ \vdots & \ddots & \ddots & \ddots & \ddots & \ddots & \vdots \\ 0 & \ddots & \ddots & \ddots & \ddots & \ddots & 0 \\ 0 & 0 & \ddots & \ddots & -l_{N-1} & l_{N-1} + l_N & -l_N \\ 0 & 0 & 0 & \cdots & 0 & -l_N & l_N \end{pmatrix} ; \quad l_{j+1} \equiv \frac{1}{x_{j+1} - x_j} . \tag{5.8}$$

In addition, with a_j and b_j as defined in (5.7), we define the vector $\mathbf{b}$, the diagonal matrix $\mathbf{A}$, and the matrix $\mathbf{M}$ by

$$\mathbf{A} \equiv \operatorname{diag}(a_j), \qquad \mathbf{b} \equiv (b_0, \ldots, b_N)^T, \qquad \mathbf{M} \equiv \mathbf{N} + \frac{1}{D_0 \gamma} \mathbf{A} . \tag{5.9}$$

The matrix $\mathbf{M}$ is clearly diagonally dominant, and hence is invertible. The solution $\mathbf{\Psi} = (\psi_0, \ldots, \psi_N)^T$ to (5.5) and (5.6), is readily calculated as

$$\mathbf{\Psi} = -\frac{\gamma}{D_0} \mathbf{M}^{-1} \mathbf{b}, \qquad \mathbf{b} = 2\tau \int_{-\infty}^{\infty} \left(w - \frac{1}{2} \left(1 - \frac{\beta}{\tau} \right) \right) \phi \, d\xi , \tag{5.10}$$

where $\boldsymbol{\phi} \equiv (\varphi_0, \ldots, \varphi_N)^T$.

Next, we define the diagonal matrix $\mathbf{K}$ and the matrix $\mathbf{P}$ by

$$\mathbf{K} = \operatorname{diag}\left(n_j^2 \alpha(x_j) \right) = \frac{6\beta^2}{\tau} \mathbf{A}, \qquad \mathbf{P} \equiv \mathbf{K} \mathbf{M}^{-1} , \tag{5.11}$$

where $\mathbf{M}$ is defined in (5.9). Then, (5.3) can be written as a vector NLEP of the form

$$\mathcal{L}_0 \boldsymbol{\phi} - \frac{\tau}{18\beta^2 D_0 \gamma} w^2 \int_{-\infty}^{\infty} \left(w - \frac{1}{2} \left(1 - \frac{\beta}{\tau} \right) \right) \mathbf{P} \boldsymbol{\phi} \, d\xi = \lambda \boldsymbol{\phi}, \quad -\infty < \xi < \infty , \tag{5.12}$$

with $\boldsymbol{\phi} \longrightarrow 0$ as $|\xi| \longrightarrow \infty$.

Next, we diagonalise $\mathbf{P}$ as $\mathbf{P} = \mathbf{Q} \mathbf{E} \mathbf{Q}^{-1}$ where $\mathbf{Q}$ is the matrix of eigenvectors of $\mathbf{P}$ and $\mathbf{E}$ is the corresponding diagonal matrix of eigenvalues. Then, upon defining $\Phi = \mathbf{Q}^{-1} \boldsymbol{\phi}$, (5.12) is diagonalised to $N + 1$ scalar NLEP's of the form

$$\mathcal{L}_0 \Phi - \frac{\mu_j}{6} w^2 (I_1 - \kappa I_2) = \lambda \Phi, \quad -\infty < \xi < \infty ; \quad \Phi \longrightarrow 0, \quad \text{as} \quad |\xi| \longrightarrow \infty , \tag{5.13}$$

where μ_j, κ, I_1, and I_2, are defined by

$$\mu_j = \left(\frac{\tau}{3\beta^2 D_0 \gamma} \right) p_j, \quad \kappa = \frac{1}{2} \left(1 - \frac{\beta}{\tau} \right), \quad I_1 = \int_{-\infty}^{\infty} w \Phi \, d\xi, \quad I_2 = \int_{-\infty}^{\infty} \Phi \, d\xi . \tag{5.14}$$

Here p_j for $j = 0, \ldots, N$ are the eigenvalues of $\mathbf{P}$. Note that since $\mathbf{A} = \tau / (6\beta^2) \mathbf{K}$ and $\mathbf{M}$ is related to $\mathbf{N}$ by (5.9), then $\mathbf{P}$ is invertible with inverse

$$\mathbf{P}^{-1} = \mathbf{N} \mathbf{K}^{-1} + \omega \mathbf{I}, \qquad \omega \equiv \frac{\tau}{6\beta^2 D_0 \gamma} . \tag{5.15}$$

Let $\sigma_0, \ldots, \sigma_N$ be the eigenvalues of matrix $\mathbf{N}\mathbf{K}^{-1}$. Then, from (5.14) and (5.15), we calculate that $\mu_j = 2\omega/(\sigma_j + \omega)$ for $j = 0, \ldots, N$.

Since the NLEP (5.13) has two separate non-local terms, it has a different form than the NLEP's studied for other reaction-diffusion systems in [22, 23, 50]. However, if we integrate (5.13) over $-\infty < \xi < \infty$, we can obtain I_2 in terms of I_1 as

$$I_2 = \frac{2 - \mu_j}{\lambda + 1 - \kappa\mu_j} I_1 \,.$$

Then, by eliminating I_2 in (5.13), we obtain a traditional NLEP with only one non-local term

$$\mathcal{L}_0\Phi - \frac{\theta_j(\lambda)}{6} w^2 \int_{-\infty}^{\infty} w\Phi \, d\xi = \lambda\Phi \,, \quad -\infty < \xi < \infty \,; \quad \theta_j(\lambda) \equiv \mu_j \frac{\lambda + 1 - 2\kappa}{\lambda + 1 - \mu_j\kappa} \,, \tag{5.16}$$

for $j = 0, \ldots, N$, with $\Phi \longrightarrow 0$ as $|\xi| \longrightarrow \infty$.

The final step in the derivation of the NLEP is to notice that θ_j is implicitly determined by μ_j, as can bee seen in (5.16). This completes the formal derivation of the NLEP, and we summarise the result as follows:

Proposition 5.1. *The stability on an $\mathcal{O}(1)$ time-scale of an $N+1$ interior patch quasi-steady-state solution is determined by the spectrum of the NLEP*

$$\mathcal{L}_0\Phi - \theta_j(\lambda)w^2 \frac{\displaystyle\int_{-\infty}^{\infty} w\Phi \, d\xi}{\displaystyle\int_{-\infty}^{\infty} w^2 \, d\xi} = \lambda\Phi \,, \qquad -\infty < \xi < \infty \,, \tag{5.17}$$

with $\Phi \longrightarrow 0$ as $|\xi| \longrightarrow \infty$, where $\theta_j(\lambda)$, for $j = 0, \ldots, N$, is given by

$$\theta_j(\lambda) \equiv \frac{2\omega(\lambda + 1 - 2\kappa)}{(\lambda + 1)(\sigma_j + \omega) - 2\kappa\omega} \,, \qquad \omega = \frac{\tau}{6\beta^2 D_0\gamma} \,, \qquad \kappa = \frac{1}{2}\left(1 - \frac{\beta}{\tau}\right) \,. \tag{5.18}$$

Here σ_j for $j = 0, \ldots, N$ are the eigenvalues of the matrix $\mathbf{N}\mathbf{K}^{-1}$, where $\mathbf{N}$ and $\mathbf{K}$ are given in (5.8) and (5.11) in terms of the instantaneous locations $x_0, \ldots, x_N$ of the patches.

Before stating our main instability result, we need to examine the analyticity of $\theta_j(\lambda)$ and some properties of the eigenvalues σ_j of $\mathbf{N}\mathbf{K}^{-1}$.

We first consider the eigenvalues σ_j for $j = 0, \ldots, N$ of $\mathbf{N}\mathbf{K}^{-1}$, which we order as $\sigma_i \leq \sigma_j$ for $i < j$. Since the sum of each row of $\mathbf{N}$ vanishes, then $\mathbf{N}\mathbf{e} = \mathbf{0}$ for $\mathbf{e} = (1, \ldots, 1)^T$, which implies that $\mathbf{N}$ is a singular matrix. Moreover, it is readily shown that the nullspace of $\mathbf{N}$ is one-dimensional, so that $\sigma_0 = 0$ is a simple eigenvalue of $\mathbf{N}\mathbf{K}^{-1}$. Next, since $\mathbf{N}$ is positive semi-definite and the matrix $\mathbf{K}$ has positive entries, it follows that $\mathbf{N}\mathbf{K}^{-1}$ is also positive semi-definite, which implies that $\sigma_j > 0$ for $1 \leq j \leq N$. To show this we calculate with $\mathbf{x} = \mathbf{K}^{1/2}\mathbf{y}$ that $\mathbf{x}^T\mathbf{N}\mathbf{K}^{-1}\mathbf{x} = \mathbf{y}^T\mathbf{K}^{1/2}\mathbf{N}\mathbf{K}^{-1/2}\mathbf{y}$. Then, since $\mathbf{K}^{1/2}\mathbf{N}\mathbf{K}^{-1/2}$ has the same spectrum as the positive semi-definite matrix $\mathbf{N}$, it follows from the equality above that $\mathbf{x}^T\mathbf{N}\mathbf{K}^{-1}\mathbf{x} \geq 0$ for all $\mathbf{x} \neq \mathbf{0}$. Hence $\mathbf{N}\mathbf{K}^{-1}$ is positive semi-definite so that $\sigma_j > 0$ for $j = 1, \ldots, N$.

Next, we examine $\theta_j(\lambda)$ in (5.18). This function has a simple pole at $\lambda = \tilde{\lambda} \equiv -1 + 2\kappa\omega/(\sigma_j + \omega)$. Using (5.18) for κ it follows that the location of this pole satisfies $\tilde{\lambda} < 0$ if and only if $-\beta\omega/\tau < \sigma_j$. Since the parameters are positive and $\sigma_j \geq 0$, it follows that $\theta_j(\lambda)$ is analytic in $\mathrm{Re}(\lambda) \geq 0$. Moreover, $1/\theta_j(\lambda)$ is analytic in $\mathrm{Re}(\lambda) \geq 0$ since the simple zero of θ_j is at $\lambda = -\beta/\tau < 0$.

With these preliminary results in hand, we now give a rigorous result for the spectrum of (5.17), which determines a sufficient condition for an instability.

Proposition 5.2. *If $\theta_j(0) < 1$ for some j, then the NLEP (5.17) has an unstable real eigenvalue in* $\mathrm{Re}(\lambda) > 0$. *If $\theta_j(0) = 1$, then $\Phi = w$ an eigenfunction of (5.17) corresponding to a zero eigenvalue.*

Proof. The proof of this rigorous result is implicit from the analysis in §3 of [51] and is sketched as follows. It is readily shown that the eigenvalues of (5.17) are the roots λ of $g(\lambda) \equiv \mathcal{C}_j(\lambda) - \mathcal{F}(\lambda) = 0$, where $\mathcal{C}_j(\lambda) \equiv 1/\theta_j(\lambda)$ and $\mathcal{F}(\lambda)$ is defined by

$$\mathcal{F}(\lambda) \equiv \frac{\int_{-\infty}^{\infty} w \left[(\mathcal{L}_0 - \lambda)^{-1} w^2 \right] d\xi}{\int_{-\infty}^{\infty} w^2 \, d\xi} \,,$$

in terms of the local operator $\mathcal{L}_0 \Psi \equiv \Psi_{\xi\xi} - \Psi + 2w\Psi$ and the homoclinic solution w. It is well-known that the local problem $\mathcal{L}_0 \Psi = \nu\Psi$ has a unique positive eigenvalue $\nu_0 > 0$ (cf. [52]). In Proposition 3.5 of [51] it is rigorously established that $\mathcal{F}(\lambda)$ has the following properties on the positive real axis:

$$\mathcal{F}(0) = 1 \,; \qquad \mathcal{F}(\lambda) \to +\infty \quad \text{as} \quad \lambda \to \nu_0^- \,; \qquad \mathcal{F}'(\lambda) > 0 \quad \text{for} \quad 0 < \lambda < \nu_0 \,.$$

With these properties for $\mathcal{F}(\lambda)$, it follows that if $\mathcal{C}_j(0) > 1$ and $\mathcal{C}_j(\lambda)$ is analytic in $\mathrm{Re}(\lambda) \geq 0$, then $\mathcal{C}_j(\lambda)$ and $\mathcal{F}(\lambda)$ must cross at some real $\lambda^\star$ in $0 < \lambda^\star < \nu_0$. Thus, $\lambda^\star$ is an unstable discrete eigenvalue of the NLEP (5.17) when $\theta_j(0) < 1$. Finally, if $\lambda = 0$ and $\theta_j(0) = 1$, then the readily-derived identity $\mathcal{L}_0 w = w^2$ shows that $\Phi = w$. ∎

This result provides a simple sufficient condition to test for an instability, with the threshold condition on the parameters obtained by setting $\theta_j(0) = 1$.

For the special case of a one-patch solution, for which $\sigma_0 = 0$, we obtain that $\theta_0 = 2$, which is independent of λ and any of the other parameters. For this special case, Lemma A and Theorem 1.4 of [52] proves for the resulting NLEP that $\mathrm{Re}(\lambda) < 0$. Therefore, a one-patch solution with a patch at any permissible location is always stable to an $\mathcal{O}(1)$ time-scale instability.

Thus, for $N > 1$, if $\theta_j(0) < 1$ for some $j = 1, \ldots, N$, then the N-patch quasi-steady-state solution is unstable. By setting $\theta_j(0) = 1$, we obtain the following main instability result:

Proposition 5.3. *Let $N > 1$. Then, the quasi-steady-state solution of (2.4) as given in Proposition 4.5 with patches at $x_0, \ldots, x_N$ is unstable on an $\mathcal{O}(1)$ time-scale if there exists at least one j in $j = 1, \ldots, N$ for which*

$$\sigma_j > \sigma_j^* \,, \qquad \text{where} \qquad \sigma_j^* \equiv \frac{1}{6\beta D_0 \gamma} \,. \tag{5.19}$$

Here σ_j for $j = 1, \ldots, N$ are the positive eigenvalues of the matrix $\mathbf{N}\mathbf{K}^{-1}$, where $\mathbf{N}$ and $\mathbf{K}$ are given in (5.8) and (5.11) in terms of the instantaneous patch locations $x_0, \ldots, x_N$. In contrast, a one-patch solution is always stable to an $\mathcal{O}(1)$ time-scale instability.

We remark that the instability criterion (5.19) can be satisfied at some later time through the slow motion of a collection of patches evolving under the DAE system in Proposition 4.5. This potential triggering of a fast $\mathcal{O}(1)$ time-scale instability through the intrinsic motion of a collection of patches is a dynamic bifurcation event, and as we shall show below it is the linear instability mechanism that triggers a nonlinear event leading to the destruction of the patches, as observed in Fig. 5.1.

We remark that although Proposition 5.2 provides a sufficient condition for instability, due to the complicated dependence of θ_j on λ, we have been unable to provide a rigorous proof that $\mathrm{Re}(\lambda) < 0$ whenever $\theta_j(0) < 1 \; \forall j$. For the two-patch example of §5.2.1, we observe from full numerical computations that there is indeed no instability when $\theta_j(0) > 1$.
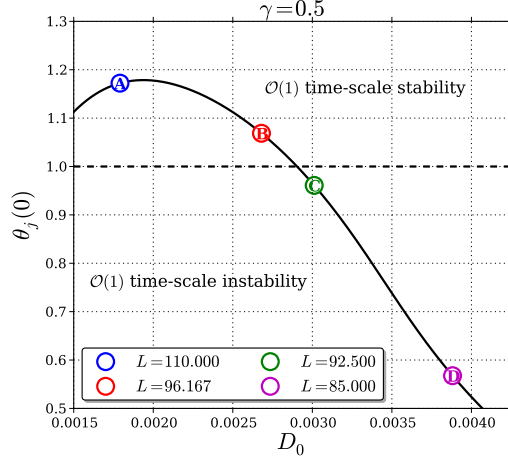
Fig. 5.2: $\mathcal{O}(1)$ time-scale competition criticality condition as D_0 is varied (corresponding to variation of L as depicted). Circled labels correspond to selected solutions with respect to their criticality value; these solutions are accordingly plotted in Fig. 5.3. Parameter set given in Table 2.1(b) with $\gamma = 0.5$ (corresponding to $k_{20} = 3.52$).

5.2. The Two-patch Case. Recall that the original bifurcation parameter is k_{20}, which models the auxin rate in the cell, while the length L of the domain is another important parameter. Since D_0 depends on L, while γ depends on k_{20}, it is convenient to write the instability threshold in (5.19) in terms of $\Lambda \equiv D_0\gamma$. In this way, (5.19) predicts that an $\mathcal{O}(1)$ time-scale instability will occur when

$$\Lambda > \Lambda^* \equiv \frac{1}{6\beta\sigma_M}, \qquad \text{where} \qquad \sigma_M \equiv \max_{1 \leq j \leq N} \{\sigma_j\}. \tag{5.20}$$

We now illustrate our result for the two-patch case of Fig. 5.1. For this case, we calculate

$$\mathbf{NK}^{-1} = \begin{pmatrix} \dfrac{l_1}{\alpha(x_0)n_0^2} & -\dfrac{l_1}{\alpha(x_1)n_1^2} \\[3mm] -\dfrac{l_1}{\alpha(x_0)n_0^2} & \dfrac{l_1}{\alpha(x_1)n_1^2} \end{pmatrix}, \qquad n_0 + n_1 = 1,$$

which has the eigenvalue $\sigma_0 = 0$. The positive eigenvalue σ_1 and corresponding eigenvector $\mathbf{q}_1$ are given explicitly by

$$\sigma_1 = \left(\frac{1}{\alpha(x_0)n_0^2} + \frac{1}{\alpha(x_1)n_1^2} \right) l_1, \qquad \text{where} \quad l_1 = \frac{1}{x_1 - x_0}; \qquad \mathbf{q}_1 = (1, -1)^T.$$

By using (5.20), we then obtain the following rigorous result:

Proposition 5.4. *A quasi-steady-state solution with exactly two interior patches has an $\mathcal{O}(1)$ time-scale competition instability when*

$$\Lambda = D_0\gamma > \Lambda^* = \frac{x_1 - x_0}{6\beta} \left(\frac{1}{\alpha(x_0)n_0^2} + \frac{1}{\alpha(x_1)(1 - n_0)^2} \right)^{-1}.$$

Here n_0, which depends on x_0 and x_1, satisfies the nonlinear algebraic equation (4.40).
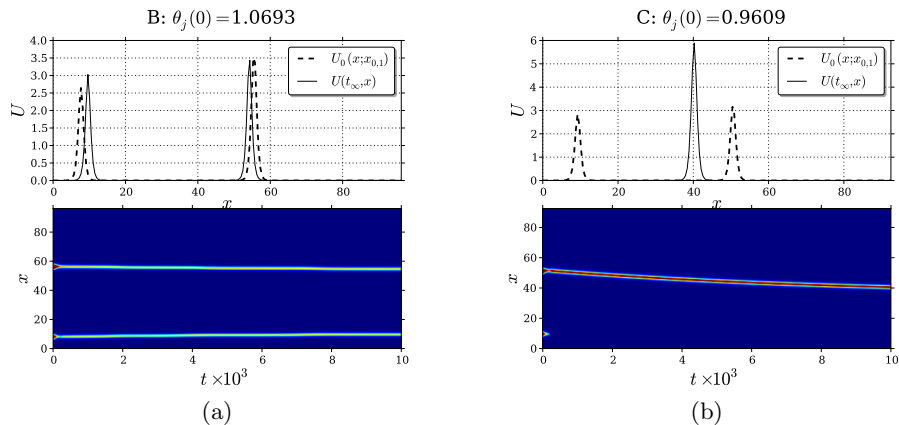
30

Fig. 5.3: $\mathcal{O}(1)$ time-scale competition instability of a two-interior-patch quasi-steady-state solution. (a) Stable solution that corresponds to label B in Fig. 5.2. (b) Unstable solution that corresponds to label C. Parameter values in D_0 for both figures are such that we are very close to the threshold $\theta_j(0) = 1$; either slightly above (a) or slightly below (b). Other parameter values are as given in Table 2.1(b).

5.2.1. Competition Threshold. This result suggests that Λ^* is smaller whenever the patches are more closely spaced, and hence it is easier to generate an instability for closely spaced patches. Furthermore, the instability eigenvector $\mathbf{q}_1$ is of sign-fluctuation type, which means that the linear instability locally increases the amplitude of one of the patches, while decreasing the amplitude of the other. We remark that, since the nonlinear algebraic equation (4.36) determining n_0 also depends on γ and D_0, it is not analytically feasible to extract a simple scaling law in terms of L and k_{20} that guarantees an instability.

To conclude this section, we test numerically the threshold given in Proposition 5.2 for the two-interior patch case. By the using parameter set given in Table 2.1(b) and a fixed value $\gamma = 0.5$, then from Proposition 4.7 we compute steady-state patch locations x_0^*, x_1^* and n_0 in terms of the parameter D_0. This provides us with a family of steady-state patch solutions in terms of D_0 for which we can either be above or below the theoretical stability threshold of $\theta_j(0) = 1$. In Fig. 5.2 we plot the numerically computed curve $\theta_j(0)$ versus D_0, which shows that $\theta_j(0) < 1$ when D_0 is too large, or equivalently when the domain length is too small. On this curve, labels A and B correspond to values of D_0 such that an $\mathcal{O}(1)$ time-scale competition stability is predicted, while for labels C and D no such instabilities are predicted. To validate this theoretical result, we calculate the quasi steady-state solution, as given in Proposition 4.5, at the parameter value of D_0 corresponding to a steady-state, and we then use it as the initial condition in the numerical computation of the full system (2.4). The full numerical results corresponding to labels B and C in Fig. 5.2 are shown in Fig. 5.3. The initial profile $U_0(x; x_{0,1})$, final profile $U(t_\infty, x)$ and $\mathcal{O}(1)$-time evolution for the stable case of the active component can be seen in Fig. 5.3(a), while instability is shown in Fig. 5.3(b). Notice, from Fig. 5.2–5.3 that the $\theta_j(0)$ values for labels B and C are both very close to the threshold value of unity, which provides a rather strict test of the stability threshold as provided by the asymptotic theory. In addition, we observe in Fig. 5.3(b) that the instability leads to the destruction of only one of the two patches, as suggested by the theoretically predicted sign-fluctuating linear instability.

5.3. Boundary-interior Patch Case. Next let us derive an instability result for the special case of a two-patch pattern consisting of a boundary patch and a single interior patch. The dynamics of this
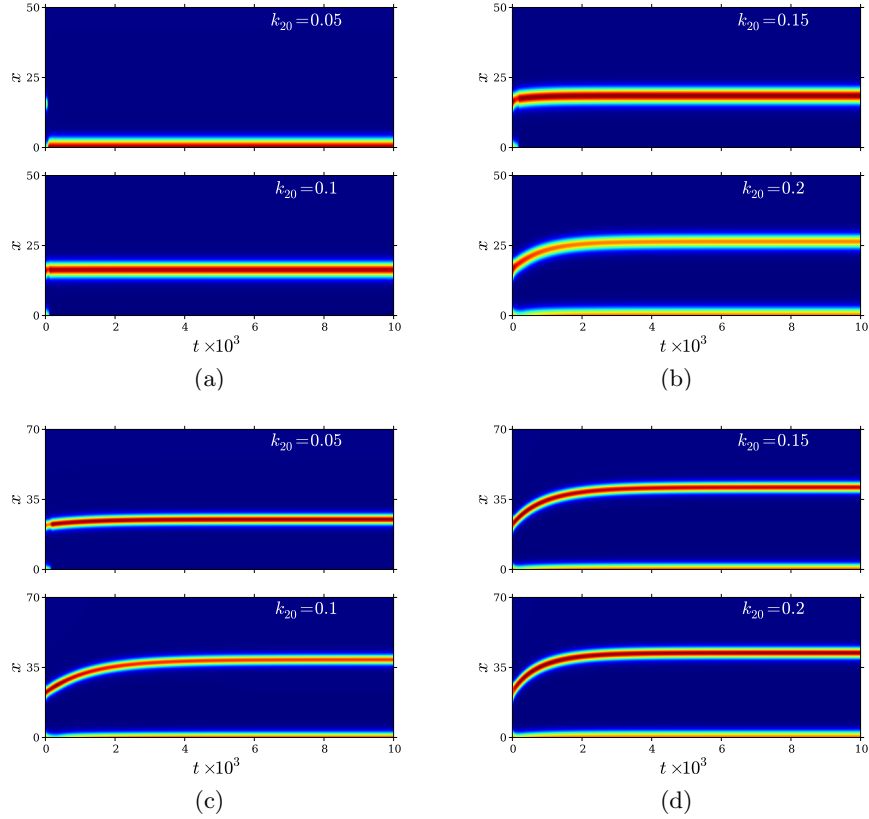
Fig. 5.4: Numerical results for an $\mathcal{O}(1)$ time-scale competition instability of a quasi-steady-state solution consisting of a boundary patch and a single interior patch. (a)-(b) $L = 50$, (c)-(d) $L = 70$, and $k_{20} = 0.05 - 0.2$ as indicated in each panel. Other parameter values as given in Table 2.1(a).

quasi-steady-state solution was characterised in Proposition 4.8. Since the analysis is very similar to that given above, we will give a brief sketch of the derivation of the NLEP and the results.

For (5.2) we look for a localized eigenfunction in the form

$$\varphi(x) \sim \varphi_0\left(\varepsilon^{-1}x\right) + \varphi_1\left(\varepsilon^{-1}(x - x_1)\right), \quad \varphi_j \longrightarrow 0 \quad \text{as} \quad |\xi| \longrightarrow \infty \,,$$

and we readily obtain that (5.3) still holds. However, in place of (5.4) we obtain that the leading-order outer approximation for ψ now satisfies

$$D_0\psi_{xx} = \left(\frac{a_1}{\gamma}\psi_1 + \gamma b_1\right)\delta(x - x_1), \quad 0 < x < 1 \,;$$

$$D_0\psi_x(0^+) = \left(\frac{a_0}{2\gamma}\psi_0 + \frac{\gamma}{2}b_0\right), \quad \psi_x(1) = 0 \,.$$

Here b_j for $j = 0, 1$ is given in (5.7), while

$$\psi_1 = \psi\left(x_0\right), \qquad \psi_0 = \psi\left(0\right), \qquad a_0 \equiv \frac{\tau n_0^2}{6\beta^2}\alpha\left(0\right), \qquad a_1 \equiv \frac{\tau n_1^2}{6\beta^2}\alpha\left(x_1\right) \,.$$

Here $n_0 = 2(1 - n_1)$ where n_1 satisfies (4.48) of Proposition 4.8.

32

We can then readily modify the stability analysis of the multi-patch case given above to again derive the NLEP (5.17) where the multiplier $\theta_j(\lambda)$ is given in (5.18). The key difference in the calculation, as compared with the derivation of the NLEP for two interior patches, is that σ_j for $j = 0, 1$ in the definition of $\theta_j(\lambda)$ of (5.18) are now the two eigenvalues of a new matrix $\mathbf{N}_b \mathbf{K}^{-1}$, where

$$\mathbf{N}_b \equiv \begin{pmatrix} 2l_1 & -2l_1 \\ -l_1 & l_1 \end{pmatrix}, \quad \text{with} \quad l_1 \equiv \frac{1}{x_1}, \qquad \mathbf{K} \equiv \begin{pmatrix} n_0^2 \alpha(0) & 0 \\ 0 & n_1^2 \alpha(x_1) \end{pmatrix}.$$

The two eigenvalues are $\sigma_0 = 0$, so that $\theta_0 = 2$ for all λ, and

$$\sigma_1 = l_1 \left(\frac{2}{n_0^2 \alpha(0)} + \frac{1}{n_1^2 \alpha(x_1)} \right).$$

The following rigorous instability threshold for the formally derived NLEP is obtained by setting $\theta_1(0) = 1$, and by replacing n_0 with $n_0 = 2(1 - n_1)$:

Proposition 5.5. *A quasi-steady-state solution with a boundary patch at $x = 0$ and an interior patch at $x = x_1$ has an $\mathcal{O}(1)$ time-scale competition instability when*

$$\Lambda = D_0 \gamma > \Lambda_b^* \equiv \frac{x_1}{6\beta} \left(\frac{1}{\alpha(x_1) n_1^2} + \frac{1}{2\alpha(0)(1 - n_1)^2} \right)^{-1}. \tag{5.21}$$

Here n_1, which depends on x_1, satisfies the nonlinear algebraic equation (4.48).

The full numerical computations of the original PDE system (2.4) shown in Fig. 5.4 reveal the effect of the domain length and the auxin parameter k_{20} on the stability of a pattern consisting of a boundary and an interior patch. The initial condition for these simulations was a quasi-steady-state solution with a boundary and an interior patch. Fig. 5.4(a) shows that only one patch survives; a boundary patch for the smaller value of k_{20}, and an interior patch for the larger k_{20} value. This is because the interior patch location x_1 is farther from the boundary when k_{20} is larger (see Fig. 4.2). However, in Fig. 5.4(b) where $k_{20} = 0.2$, the two patches survive. In Figures 5.4(c) and 5.4(d) where L is larger, again both patches survive. In Fig. 5.4(d), the slow evolution of the interior patch is evident over a long time-scale.

6. Conclusion. In this paper we have performed a thorough mathematical analysis of an inhomogeneous reaction-diffusion system that has previously been derived as a model for root hair formation in plants, and shown to match both the behaviour of wild type and mutants in biologically plausible parameter regions. It is worthwhile pointing out some further predictions of analysis that are likely to have a bearing on the biology.

- As the two key parameters auxin and cell length increase in the developing root hair cell, the process of forming an active-ROP patch that will go on to bulge into a root hair bud proceeds via a number of abrupt transitions, interspersed with periods of slow drift.
- The first abrupt transition is to form a patch of active ROP at the apical end of the cell. The next transition is for this patch to become unstable and for a new patch to form in the interior of the cell body, strongly biassed towards the apical end. This latter transition is hysteretic, which means that once such a transition is triggered, a slight reversal of the steps that caused it will not undo the transition. This is likely to be biologically important, since in reality all biochemical processes will feature stochastic fluctuations and will be susceptible to influences from the plant's external environment. Hence the transition will be robust to both stochastic fluctuations and also exogenous influence.

- The formation of multiple root hairs could be construed as a matter of timing. If too much auxin arrives too quickly, before secondary processes have caused a single ROP patch to lock into position as the emerging hair is formed, then there can be a further transition to multiple patch states. Similarly, if there is excess auxin or greater cell lengthening, but insufficient to cause multiple root hairs, then we should expect that there will be further drift of the wild-type patch location from the apical end.
- Finally, through the asymptotic analysis and the two-parameter bifurcation diagrams, we have shown that the process we have described is robust to relaxation of some of the underlying assumptions that have gone into the model. At present the auxin dependency of the activation process is only hypothesised. However we can see that many of the other parameters could play a similar role to that of k_2 in controlling this hysteretic transition process. Also, the precise shape of the auxin gradient is not important, providing it is monotically decreasing.

Each of these predictions is ripe for further experimental investigation.

This paper also sheds light more generally on the mathematics of pattern formation. It seems significant that this model without a spatial gradient is in the regime in which Turing instabilities occur. Yet, each of these instabilities are *subcritical*. Note that a subcritical initial patterning instability is one of the ingredients of the theory of homoclinic snaking on an infinite domain, see e.g. [3, 6]. This connection will be explored in future work. Without the spatial gradient the model still forms localized patterns, the role of the gradient seems just to be that of controlling the location of the localized pattern, through the slow-time-scale patch-drift equation.

Another direction that will be explored in future work will be the extension of the ideas in this paper to higher spatial dimensions. The biological process described here takes place on the surface of a long, thin epidermal cell. Preliminary results suggest similar behaviour occurs for the same model posed on a long, thin mathematical domain. Further issues to be addressed though involve the interplay between lateral stripes and spot-like states, the richer zoo of possible localized states, further instability mechanisms and how these are affected by transverse properties of the morphogen gradient.

REFERENCES

[1] D. L. Benson, J. A. Sherrat, and P. K. Maini, *Diffusion driven instability in a inhomogeneous domain*, Bull. Math. Biol., 55 (1993), pp. 365–384.

[2] F. Berger, C.–Y. Hung, L. Dolan, and J. Schiefelbein, *Control of cell division in the root epidermis of Arabidopsis thaliana*, Dev. Biol., 194 (1998), pp. 235–245.

[3] J. Burke and E. Knobloch, *Snakes and ladders: Localized states in the Swift–Hohenberg equation*, Physics Letters A, 360 (2006), pp. 681–688.

[4] X.R. Bustelo, V. Sauzeau, and I.M. Berenjeno, *GTP-binding proteins of the Rho/Rac family: regulation, effectors and functions in vivo*, Bioessays, 29 (2007), pp. 356–370.

[5] W. Chen and M.J. Ward, *The stability and dynamics of localized spot patterns in the two-dimensional Gray–Scott model*, SIAM J. Applied Dynamical Systems, 10 (2011), pp. 582–666.

[6] J.H.P. Dawes, *Localized pattern formation with a large-scale mode: Slanted snaking*, SIAM J. Applied Dynamical Systems, 7 (2008), pp. 186–206.

[7] E. Doedel, B.E. Oldeman, A.R. Champneys, f. Dercole, T. Fairgrieve, Y. Kuznetsov, X. Wang, and C. Zhang, *AUTO-07P: Continuation and bifurcation software for ordinary differential equations*. http://www.dam.brown.edu/people/sandsted/auto/auto07p.pdf, 2012.

[8] A. DOELMAN AND T.J. KAPER, *Semistrong pulse interactions in a class of couple reaction-diffusion equations*, SIAM J. Applied Dynamical Systems, 2 (2003), pp. 53–96.

[9] A. DOELMAN, T.J. KAPER, AND P.A. ZEGELING, *Pattern formation in the one-dimensional Gray–Scott model*, Nonlinearity, 10 (1997), pp. 523–563.

[10] L. DOLAN, C. DUCKETT, C. GRIERSON, P. LINSTEAD, K. SCHNEIDER, E. LAWSON, C. DEAN, S. POETHIG, AND K. ROBERTS, *Clonal relations and patterning in the root epidermis of Arabidopsis*, Development, 120 (1994), pp. 2465–2474.

[11] V. DUFIET AND J. BOISSONADE, *Conventional and unconventional Turing patterns*, J. Chem. Phys., 96 (1992), pp. 662–673.

[12] J. EHRT, J. D. M. RADEMACHER, AND M. WOLFRUM, *First and second order semi-strong interaction of pulses in the Schnakenberg model*. Draft version, 2012.

[13] B. ERMENTROUT, *Simulating, Analyzing, and Animating Dynamical Systems: A Guide to XPPAut*, SIAM, 2002.

[14] S. ETIENNE–MANNEVILLE AND A. HALL, *Rho GTPases in cell biology*, Nature, 420 (2002), pp. 629–635.

[15] J. FOREMAN AND L. DOLAN, *Root hairs as a model system for studying plant cell growth*, Annals of Botany, 88 (2001), pp. 1–7.

[16] G. FRESHOURS, R. P. CLAY, M. S. FULLER, P. ALBERSHEIM, A. G. DARVILL, AND M. G. HAHN, *Developmental and tissue-specific structural alterations of the cell-wall polysaccharides of Arabidopsis thaliana roots*, Plant. Physiol., 110 (1996), pp. 1413–1429.

[17] M. E. GALAWAY, J. D. MASUCCI, A.M. LLOYD, V. WALBOT, R. W. DAVIS, AND J. W. SCHIEFELBEIN, *The TTG gene is required to specify epidermal cell fate and cell patterning in the Arabidopsis root*, Dev. Biol., 166 (1994), pp. 740–754.

[18] T. GLIMM, J. ZHANG, AND Y.–Q. SHEN, *Interaction of Turing patterns with an external linear morphogen gradient*, Nonlinearity, 22 (2009), pp. 2541–2560.

[19] T. GLIMM, J. ZHANG, Y.–Q. SHEN, AND S. NEWMAN, *Reaction-diffusion systems and external morphogen gradients: the two-dimensional case, with an application to skeletal pattern formation*, Bull. Math. Biol., 74 (2012), pp. 666–687.

[20] V.A. GRIENEISEN, A.F. MAREE, P. HOGEWEG, AND B. SCHERES, *Auxin transport is sufficient to generate a maximum and gradient guiding root growth*, Nature, 449 (2007), pp. 1008–1013.

[21] C. GRIERSON AND J. SCHIEFELBEIN, *The Arabidopsis Book*, American Society of Plant Biologist, 2002.

[22] D. IRON AND M.J. WARD, *The dynamics of multi-spikes solutions to the one-dimensional Gierer–Meinhardt model*, SIAM J. Appl. Math., 62 (2002), pp. 1924–1951.

[23] D. IRON, J. WEI, AND M. WINTER, *Stability analysis of Turing patterns generated by the Schnakenberg model*, J. Math. Biol., 49 (2004), pp. 358–390.

[24] A.R. JONES, E.M. KRAMER, K. KNOX, R. SWARUP, M.J. BENNETT, C.M. LAZARY, H.M. OTTOLINE LEYSER, AND C.S. GRIERSON, *Auxin transport through non-hair cells sustains root-hair development*, Nat. Cell. Biol., 11 (2009), pp. 78–84.

[25] M. JONES AND N. SMIRNOFF, *Nuclear dynamics during the simultaneous and sustained tip growth of multiple root hairs arising from a single root epidermal cell*, J. of Exp. Bot., 57 (2006), pp. 4269–4275.

[26] M. A. JONES, J–J. SHEN, Y. FU, H. LI, Z. YANG, AND C. GRIERSON, *The Arabidopsis Rop2 GTPase is a positive regulator of both root hair initiation and tip growth*, The Plant Cell, 14 (2002), pp. 763–776.

[27] T. KOLOKOLNIKOV, M.J. WARD, AND J. WEI, *Spot self-replication and dynamics for the Schnakenberg model in a two-dimensional domain*, J. Nonlinear Sci., 19 (2009), pp. 1–56.

[28] E. M. KRAMER, *PIN and AUX/LAX proteins: their role in auxin accumulation*, Trends. Plant Sci., 9 (2004), pp. 578–582.

[29] A. D. LANDER, *Pattern, growth, and control*, Cell, 144 (2011), pp. 955–969.

[30] P. K. MAINI, D. L. BENSON, AND J. A. SHERRAT, *Pattern formation in reaction-diffusion models with spatially inhomogeneous diffusion coefficients*, IMA Journal of Mathematics Applied in Medicine & Biology, 9 (1992), pp. 197–213.

[31] P. K. MAINI, K. J. PAINTER, AND H. N. PHONG–CHAU, *Spatial pattern formation in chemical and biological systems*, J. Chem. Soc., Faraday Trans., 93 (1997), pp. 3601–3610.

[32] K. MATTIES AND C.E. WAYNE, *Wave pinning in strips*, Proceedings of the Royal Society of Edinburgh, 136A (2006), pp. 971–995.

[33] A.K. MOLENDIJK, F. BISCHOFF, C.S.V. RAJENDRAKUMAR, J. FRIML, AND M. BRAUN, *Arabidopsis thaliana ROP GTPases are localized to tips of root hairs and control polar growth*, EMBO J., 20 (2001), pp. 2779–2788.

[34] Y. MORI, A. JILKINE, AND L. EDELSTEIN–KESCHET, *Wave-pinning and cell polarity from a bistable reaction-diffusion system*, Biophysical Journal, 94 (2008), pp. 3684–3697.

[35] J.D. MURRAY, *Mathematical Biology II: spatial models and biomedical applications*, Springer–Verlag New York Inc., New York, 3rd. ed., 2002.

[36] S. NAGAWA, T. XU, AND Z. YANG, *Rho GTPases in plants: conservation and invention of regulators and effectors*, Small GTPases, 1 (2010), pp. 78–88.

[37] Y. NISHIURA, Y. OYAMA, AND K.–I. UEDA, *Dynamics of traveling pulses in heterogeneous media of jump type*, Hokkaido Mathematical Journal, 36 (2007), pp. 207–242.

[38] K.M. PAGE, P. MAINI, AND N.A.M. MONK, *Pattern formation in spatially heterogenous Turing reaction-diffusion models*, Physica D, 181 (2003), pp. 80–101.

[39] ———, *Complex pattern formation in reaction-diffusion systems with spatially varying parameters*, Physica D, 202 (2005), pp. 95–115.

[40] H.–O. PARK AND E. BI, *Central roles of small GTPases in the development of cell polarity in yeast and beyond*, Microbiol. Mol. Biol. Rev., 71 (2007), pp. 48–96.

[41] R.J.H. PAYNE AND C.S. GRIERSON, *A theoretical model for ROP localisation by auxin in Arabidopsis root hair cells*, PLoS ONE, 4 (2009), p. e8337. doi:10.1371/journal.pone.0008337.

[42] J. D. M. RADEMACHER, *First and second order semi-strong interaction in reaction-diffusion systems*, SIAM J. Applied

Dynamical Systems, 12 (2013), pp. 175–203.

[43] R.W. Ridge and A.M.C. Emons, eds., *Root Hairs: cell and molecular biology*, Springer, Berlin, Heidelberg, 2000.

[44] N. S. Savage, T. Walker, Y. Wieckowski, J. Schiefelbein, L. Dolan, and N.A.M. Monk, *A mutual support mechanism through intercellular movement of CAPRICE and GLABRA3 can pattern the Arabidopsis root epidermis*, PLoS Biology, 6 (2008), p. e235. doi:10.1371/journal.pbio.0060235.

[45] J. Schnakenberg, *Simple chemical reaction systems with limit cycle behaviour*, J. Theor. Biol., 81 (1979), pp. 389–400.

[46] TAIR, *The arabidopsis information resource.* http://www.arabidopsis.org/index.jsp, October 2012.

[47] P. van Heijster, A. Doelman, T. J. Kaper, Y. Nishiura, and K.–I. Ueda, *Pinned fronts in heterogeneous media of jump type*, Nonlinearity, 24 (2011), pp. 127–157.

[48] J. A. Vastano, J. E. Pearson, W. Horsthemke, and H. L. Swinney, *Chemical pattern formation with equal diffusion coefficients*, Physics Letters A, 124 (1987), pp. 320–324.

[49] M.J. Ward, D. McInerney, P. Houston, D. Gavaghan, and P. Maini, *The dynamics and pinning of a spike for a reaction-diffusion system*, SIAM J. Appl. Math., 62 (2002), pp. 1297–1328.

[50] M. J. Ward and J. Wei, *The existence and stability of asymmetric spike patterns for the Schnakenberg model*, Studies in Advance Mathematics, 109 (2002), pp. 229–264.

[51] ——, *Hopf bifurcation and oscillatory instabilities of spike solutions for the one-dimensional Gierer–Meinhardt model*, J. Nonlinear Sci., 13 (2003), pp. 209–264.

[52] J. Wei, *On single interior spike solutions for the Gierer–Meinhardt system: uniqueness and stability estimates*, Europ. J. Appl. Math., 10 (1999), pp. 353–378.

[53] J. Wei and M. Winter, *Spikes for the Geirer–Meinhardt system with discontinuous diffusion coefficients*, Nonlinear Science, 19 (2009), pp. 301–339.

[54] X. Yuan, T. Teramoto, and Y. Nishiura, *Heterogeneity-induced defect bifurcation and pulse dynamics for a three-component reaction-diffusion system*, Phys. Rev. E, 75 (2007), p. 036220.